J. Fluid Mech. (2014), *vol.* 743, *pp.* 170–201.
doi:10.1017/jfm.2014.54

Computational modelling of flow through prosthetic heart valves using the entropic lattice-Boltzmann method

B. Min Yun[1], L. P. Dasi[2], C. K. Aidun[1,3] and A. P. Yoganathan[1,4,†]

[1]G. W. Woodruff School of Mechanical Engineering, Georgia Institute of Technology, 500 10th Street NW, Atlanta, GA 30318, USA

[2]Department of Mechanical Engineering, Colorado State University, Campus Delivery 1374, Fort Collins, CO 80523, USA

[3]Parker H. Petit Institute for Bioengineering and Bioscience, Georgia Institute of Technology, 315 Ferst Drive, Atlanta, GA 30332, USA

[4]Wallace H. Coulter Department of Biomedical Engineering, Georgia Institute of Technology and Emory University, 313 Ferst Drive, Atlanta, GA 30332, USA

(Received 9 March 2013; revised 5 December 2013; accepted 17 January 2014; first published online 3 March 2014)

Previous clinical, *in vitro* experimental and *in silico* simulation studies have shown the complex dynamics of flow through prosthetic heart valves. In the case of bileaflet mechanical heart valves (BMHVs), complex flow phenomena are observed due to the presence of two rigid leaflets. A numerical method for this type of study must be able to accurately simulate pulsatile flow through BMHVs with the inclusion of leaflet motion and high-Reynolds-number flow modelling. Consequently, this study aims at validating a numerical method that captures the flow dynamics for pulsatile flow through a BMHV. A 23 mm St. Jude Medical (SJM) Regent^{TM} valve is selected for use in both the experiments and numerical simulations. The entropic lattice-Boltzmann method is used to simulate pulsatile flow through the valve with the inclusion of reverse leakage flow, while prescribing the flowrate and leaflet motion from experimental data. The numerical simulations are compared against experimental digital particle image velocimetry (DPIV) results from a previous study for validation. The numerical method is shown to match well with the experimental results quantitatively as well as qualitatively. Simulations are performed with efficient parallel processing at very high spatiotemporal resolution that can capture the finest details in the pulsatile BMHV flow field. This study validates the lattice-Boltzmann method as suitable for simulating pulsatile, high-Reynolds-number flows through prosthetic devices for use in future research.

Key words: biomedical flows, computational methods, vortex dynamics

1. Introduction

Heart valves are essential to the cardiovascular circulatory system and function by maintaining unidirectional flow of blood in the heart. Native heart valves may

† Email address for correspondence: ajit.yoganathan@bme.gatech.edu

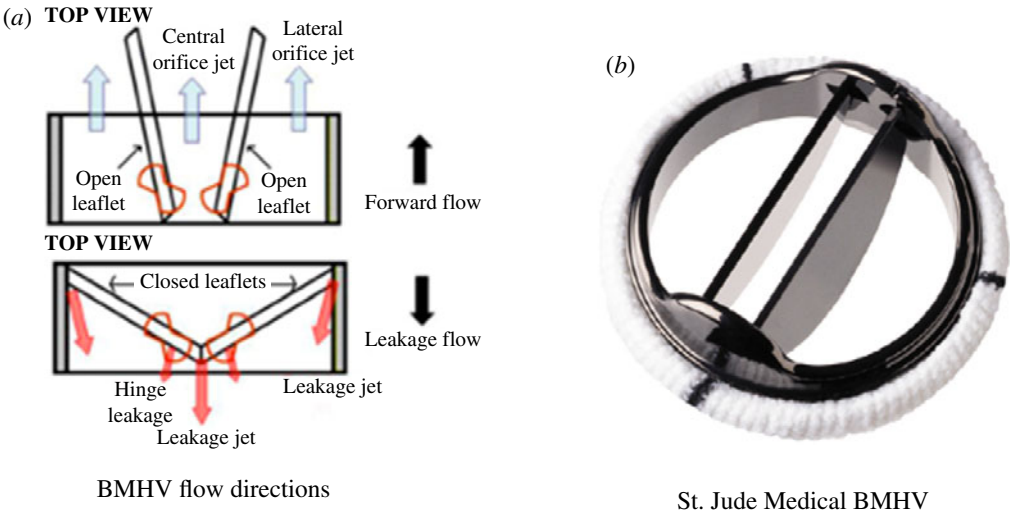

BMHV flow directions

St. Jude Medical BMHV

FIGURE 1. Schematic of forward and reverse BMHV flows and the popular SJM valve design: (*a*) BMHV flow directions; (*b*) St. Jude Medical BMHV.

become defective due to congenital birth defects or disease. Prosthetic valves have been used for over 50 years to replace defective valves, and mechanical heart valves are currently one of the most popular prosthetic valve designs (Black & Drury 1994). Among mechanical heart valves, the bileaflet mechanical heart valve (BMHV) is the most popular design and accounts for 80 % (Yoganathan *et al.* 2003) of implanted mechanical heart valves. Its popularity over other prosthetic heart valves is mainly due to its superior durability, function and bulk flow hemodynamics.

Figure 1(*a*) shows a schematic of a BMHV that shows the range of leaflet motion, the hinges to which the leaflets are attached, and flow regions. The circular wall of the valve is referred to as the valve housing. During forward flow, most of the blood flows through three orifices formed by the open leaflets (figure 1(*a*)). The three forward flow jets are through the two lateral orifices, and the central orifice. In reverse flow, there is leakage flow through the hinges, the gap between the closed leaflets and valve housing and through the central b-datum plane.

Despite improvements in design evolution, BMHVs still cause serious complications such as platelet activation and thromboembolism (Giersiepen *et al.* 1990; Grunkemeier & Anderson Jr 1998). These complications are thought to be due to non-physiologic shear stress levels imposed on blood elements by complex flows through BMHVs (Ellis *et al.* 1996; Ellis & Yoganathan 2000). This may lead to thrombus formation in the valves, and emboli may detach and become lodged in smaller blood vessels, leading to stroke and death. Various experimental studies have been performed on flow through prosthetic heart valves to study the complex flow dynamics (Lim *et al.* 1994; Manning *et al.* 2003). A common limitation of experimental studies is the lack of optical access within the valve, particularly close to the leaflets. This prevents detailed and full-view analysis of the complex flows caused by the BMHV geometry.

An advantage of computational fluid dynamics (CFD) in exploring BMHV flows is the ability to model three-dimensional flows with high spatiotemporal resolution, whereas experimental studies are mostly limited to data in 2D planes. The vorticity dynamics in pulsatile BMHV flows were explored in one dual

experimental-computational study (Dasi *et al.* 2007). 3D vorticity dynamics was explored computationally, showing rich, complex three-dimensional vortex structures with greater clarity than experimental results. Computational simulations of flow through BMHVs have also included dynamic leaflet motion using two-way fluid–solid interaction (FSI), including one study by De Tullio *et al.* (2010) that employed an immersed boundary method to simulate pulsatile 3D flow through a BMHV. Computational methods have also expanded in modelling beyond simplified *in vitro* geometries, focusing on more physiological geometries that include bends in the domain and more anatomical features. Studies by Borazjani *et al.* (Borazjani, Ge & Sotiropoulos 2008; Borazjani & Sotiropoulos 2010) examined pulsatile 3D flow through a BMHV in an anatomic aorta, characterizing the effect of realistic geometries on the BMHV flow fields.

Although blood damage experiments are possible for flow through BMHVs or BMHV-like geometries (Fallon *et al.* 2008), these experiments can only give bulk blood damage results and cannot pinpoint the locations and times of greatest damage. CFD studies have employed particle tracking methods in order to quantify blood damage in these flows (Simon *et al.* 2010; Xenos *et al.* 2010). However, these methods are limited in modelling only single-phase flows, and evaluating fluid shear stresses as the assumed shear stresses experienced by platelets. CFD studies have also been performed characterizing complex three-dimensional flows through the hinge (Simon *et al.* 2009), and have also included suspended platelets to track blood element damage in BMHV 3D hinge flows (Wu *et al.* 2011; Yun *et al.* 2012).

CFD can exploit parallel processing capabilities and large computational cluster resources to model high-resolution, 3D, pulsatile flows through prosthetic heart valve designs with the inclusion of suspended blood elements for accurately tracking damage. This will allow for the improved understanding of how blood damage occurs in these flows and lead to the eventual optimization of various prosthetic device designs in order to reduce complications. In order to capture the smallest relevant scales in pulsatile, high-Reynolds-number BMHV flows, high spatiotemporal resolution is required, which lead to high computational expenses. A true suspension flow solver is also required to accurately quantify blood element damage. To accomplish these goals, an efficient, parallel, multiscale suspension flow modelling method is required. This method must first be validated with experimental flow data in order to show that it can accurately model complex, pulsatile BMHV flows before being used to assess blood element damage.

The objective of this study is to validate a numerical entropic lattice-Boltzmann method (LBM) for modelling pulsatile, high-Reynolds-number BMHV flows by comparison with experimental data. First, comparisons are made for cases of steady forward flow through a BMHV. Both laminar and turbulent regimes are modelled for the steady flow cases to show the accuracy of the numerical method to model different Reynolds numbers. Next, pulsatile flow through a BMHV is simulated and results are compared to pulsatile flow experimental data both quantitatively and qualitatively to demonstrate the ability of the numerical method to capture pulsatile, high-Reynolds-number BMHV flows.

The paper is organized as follows. In § 2, we present the entropic LBM for simulating flow, the experimental and numerical design, and details of the validation with experiments. In § 3, we simulate steady and pulsatile flow past a BMHV and show comparisons with experiments. In § 4, we discuss the results of our simulations and their implications, as well as the future research use of the numerical method. Concluding remarks are made in § 5.

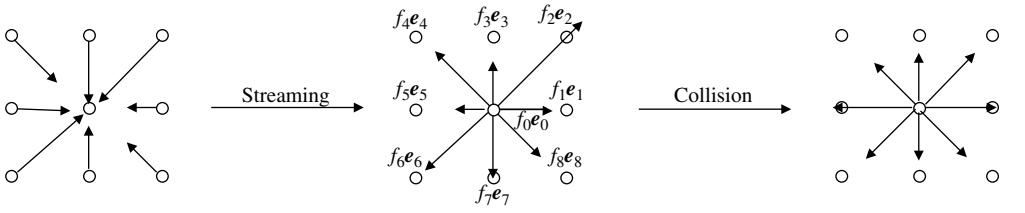

FIGURE 2. Simplified illustration of streaming and collision processes for the LBM, shown for a 2D, nine-vector model.

2. Methodology

The numerical flow methodology for this study is based on the LBM. The appeal of LBM lies in the nature of its local, linear calculations, which make it highly efficient when used for parallel simulations. FSI is derived from the lattice-Boltzmann standard bounce-back (SBB) methodology as described by Aidun *et al.* (Aidun & Lu 1995; Aidun, Lu & Ding 1998; Aidun & Clausen 2010) and Macmeccan *et al.* (2008). A modification to the LBM to allow for very high-Reynolds-number flow simulations is implemented by the entropic lattice-Boltzmann (ELB) method (Keating *et al.* 2007). These numerical methodologies have been extensively validated in the cited previous studies with a variety of single-phase flow simulations as well as suspended particle flow validation simulations.

2.1. *LBM*

The LBM is a direct numerical simulation (DNS) method used for solving fluid flow, and is based on kinetic gas theory. The review by Aidun & Clausen (2010) presents an overview of LBMs for modelling complex flows. The method described by Aidun *et al.* (1998), as employed in this study, is a single-relaxation method. The method is normally applicable to low- to moderately low-Reynolds-number flows.

In the LBM, the fluid is modelled as a continuous distribution of fictitious fluid particles that exist on a fixed regular lattice grid that discretizes 3D velocity space. Each node on this grid is linked to neighbouring nodes through lattice velocity vectors. In the simulations of this study, a 3D, 19-vector Cartesian velocity set (D3Q19) is employed.

The fluid particle distribution changes with time through processes known as 'streaming' and 'collision' (figure 2). In streaming, fluid particles move to neighbouring grid nodes that are connected by lattice velocity links. In collision, fluid particles arriving at a node collide with each other and change the fluid particle distribution at that node. These processes dictate the time evolution of the fluid particle distribution at each node and only require knowledge of the fluid particle distributions at neighbouring nodes, making all calculations localized in space. The lattice-Boltzmann equation, using the single-relaxation-time Bhatnagar–Gross–Krook (BGK) collision operator, is given as

$$f_i(\boldsymbol{r}+\boldsymbol{e}_i, t+1) = f_i(\boldsymbol{r}, t) - \frac{1}{\tau}(f_i(\boldsymbol{r}, t) - f_i^{(0)}(\boldsymbol{r}, t)), \tag{2.1}$$

where f_i is the fluid particle distribution function, $f_i^{(0)}$ is the equilibrium distribution function, $\boldsymbol{r}$ is the spatial location of the fluid particles, $\boldsymbol{e}_i$ is the lattice velocity vector,

τ is the single relaxation time and t is time. The index i varies from 0 to 18 for the D3Q19 model, where $i=0$ is the rest particle.

The solution of the lattice-Boltzmann equations converges to the solution of the incompressible Navier–Stokes equations for fluid flow when the lattice spacing is much smaller than a characteristic simulation length scale. The method uses a pseudo-sound speed of $c_s = \sqrt{1/3}$. The relation between kinematic viscosity ν and single relaxation time τ is

$$\tau = \left(\frac{1}{c_s}\right)^2 \nu \left(\frac{\Delta t}{(\Delta x)^2}\right) + 0.5, \tag{2.2}$$

where the time and length discretizations are normalized such that $\Delta t = \Delta x = 1$.

The equilibrium distribution function is given by

$$f_i^{(0)}(\boldsymbol{r}, t) = \rho w_i \left[1 + \frac{1}{c_s^2}(\boldsymbol{e}_i \cdot \boldsymbol{u}) + \frac{1}{2c_s^4}(\boldsymbol{e}_i \cdot \boldsymbol{u})^2 - \frac{1}{2c_s^2}(\boldsymbol{u} \cdot \boldsymbol{u})\right], \tag{2.3}$$

where ρ is density, $\boldsymbol{u}$ is macroscopic fluid velocity and w_i are the lattice weights. The lattice weights for the D3Q19 model are $w_i = 0$ for $i = 0$, $w_i = 1/18$ for non-diagonal lattice velocity directions and $w_i = 1/36$ for the diagonal directions.

The macroscopic flow properties (density, velocity and pressure) are recovered by the moments of the equilibrium distribution function, and are given as

$$\rho = \sum_i f_i^{(0)}(\boldsymbol{r}, t) \tag{2.4}$$

$$\rho \boldsymbol{u} = \sum_i f_i^{(0)}(\boldsymbol{r}, t)\ \boldsymbol{e}_i \tag{2.5}$$

$$c_s^2 \rho \boldsymbol{I} + \rho \boldsymbol{u}\boldsymbol{u} = \sum_i f_i^{(0)}(\boldsymbol{r}, t)\ \boldsymbol{e}_i \boldsymbol{e}_i, \tag{2.6}$$

where $\boldsymbol{I}$ is the identity tensor. In the LBM, the pressure is proportional to the density by $p = c_s^2 \rho = \rho/3$.

The boundaries between the fluid and solid surfaces are connected via 'links', and the FSIs are dealt with via the SBB method. As the BGK collision operator and all streaming are localized in space, parallelization of the LBM is straightforward. For complete details on the LBM or SBB, please refer to Aidun *et al.* (1998) and Aidun & Clausen (2010).

2.2. *ELB*

The LBM is a DNS method for solving fluid flow and thus no special turbulence modelling is required. However, when the flow velocity or its spatial gradient becomes too large for the lattice, numerical instabilities arise in the form of negative fluid distribution values. These instabilities become a significant problem when simulating higher-Reynolds-number flows. In order to eliminate these instabilities, a special ELB method has been proposed for modelling high-Reynolds-number flows (Keating *et al.* 2007). Briefly, a discrete H-theorem constraint is applied which enforces universal positive-definiteness on all particle distribution values. These methods lead to stable explicit algorithms even at very low viscosities, allowing for the modelling of very

high-Reynolds-numbers with good accuracy. The ELB equation is a modification of the single-relaxation lattice-Boltzmann equation, and is written as

$$f_i(\boldsymbol{r}+\boldsymbol{e}_i, t+1) = f_i(\boldsymbol{r}, t) - \frac{\gamma}{2\tau}(f_i(\boldsymbol{r}, t) - f_i^{(0)}(\boldsymbol{r}, t)) \tag{2.7}$$

where γ is the non-trivial root of

$$H[\boldsymbol{f}] = H[\boldsymbol{f} - \gamma(\boldsymbol{f} - \boldsymbol{f}^{(0)})]. \tag{2.8}$$

The term $H[\boldsymbol{f}]$ is the discrete form of the standard continuum Boltzmann H function, given as

$$H[\boldsymbol{f}] = \sum_{i=0}^{N-1} f_i \ln\left(\frac{f_i}{w_i}\right) \tag{2.9}$$

where N is the number of lattice velocity directions (19 for the D3Q19 model). The ELB method is only applied at nodes where instabilities are determined for the fluid particle distributions. The γ root value is determined in (2.8) by using a rapidly converging Newton–Raphson procedure at each time iteration for unstable grid points. After the ELB method stabilizes a fluid grid node, the original single-relaxation lattice-Boltzmann equation (2.1) is again employed. More details on ELB methods can be found in the methodology paper by Keating *et al.* (2007).

2.3. *Experimental work*

To validate the numerical method as appropriate for modelling pulsatile BMHV flows, comparisons are made between the numerical simulations and previous experimental data. *In vitro* particle image velocimetry (PIV) experiments were performed of steady flow past fully open leaflets of an SJM valve (figure 1*b*) in the aortic position using a blood analogue fluid (Ge *et al.* 2005). An averaged 2D flow field was determined over 100–200 samples for various Reynolds numbers and used for validation.

The same *in vitro* flow loop was used to recreate pulsatile flow through a SJM valve throughout the cardiac cycle (Dasi *et al.* 2007). A cardiac cycle with a period of 860 ms was employed, corresponding to 70 beats min^{-1}. The mean flow rate was adjusted to 4.5 l min^{-1} with a peak flow rate of 25.0 l min^{-1} and a forward flow duration of approximately 340 ms. A blood analogue fluid was used that matched the kinematic viscosity of whole human blood (3.5×10^{-6} m^2 s^{-1}), and was composed of 79 % saturated aqueous sodium iodide, 20 % glycerin and 1 % water by volume. The density of this blood analogue was approximately 1620 kg m^{-3}, as compared with 1060 kg m^{-3} for whole human blood. This was necessary to match the refractive index of the fluid to the experimental chamber for optimal visualization. Although the blood analogue density does not match that of whole blood, matching kinematic viscosity was determined as most important to modelling pulsatile BMHV flows.

Figure 3 shows a schematic of the SJM valve in the experimental flow chamber. The chamber was made of rigid straight tubes with a diameter of 25.4 mm. The valve itself is a 23 mm SJM valve with an inner diameter of 21.4 mm. Downstream of the valve on the aortic side is a sudden axisymmetric expansion to a diameter of 31.75 mm representing the idealized aortic sinus root immediately downstream of the aortic valve. Figure 3 shows the longitudinal cutplanes at which PIV measurements are made, perpendicular to the leaflets and in the centre of the valve in the side view. The spatial resolution of the PIV flow data used for comparison is approximately 134 μm. Figure 4 shows the ensemble-averaged flow rate and leaflet angle as they vary throughout the cardiac cycle for the pulsatile flow experiments. More descriptions of the experimental set-up can be found in the literature (Dasi *et al.* 2007).

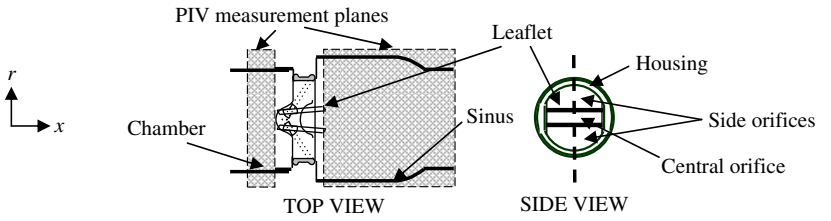

FIGURE 3. Experimental set-up.

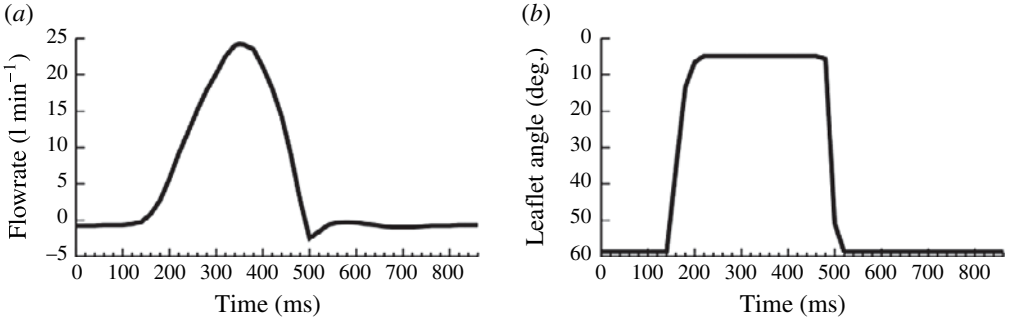

FIGURE 4. Flowrate and leaflet angle variation for one cardiac cycle. (*a*) Flowrate curve. (*b*) Leaflet angle curve.

2.4. *Numerical set-up and boundary conditions*

The exact *in vitro* experimental set-up was recreated computationally using micro computed tomography (microCT) and is shown in figure 5. A quarter-cut scan of the valve was employed and then reflected twice to create a perfectly symmetric geometry across the two cross-section axes. For comparison with experiments for steady flow, the numerical fluid domain employed uniform 3D grid spacing with a spatial resolution of 160 μm and a temporal resolution of 4.8 μs per numerical timestep. The flow domain is discretized into a mesh of 2432 × 204 × 204 grid nodes at this 160 μm spatial resolution for the axial and cross-sectional directions, respectively. Although the spatial resolution is not high enough to resolve flow through the hinge regions or through the gap between the closed leaflets and the valve housing, it is sufficient to resolve the bulk flow through the valve while minimizing computational costs. In addition, the PIV flow data-averaged flow features due to the 200 μm laser sheet thickness and laser pulse separation. Thus the 160 μm computational spatial resolution is deemed suitable for capturing all important bulk flow features for experimental comparison. This resolution is employed for steady flow and qualitative pulsatile flow comparisons.

Although the two gap regions are important in a complete study of BMHV flows, only the bulk flow field is of interest for this specific study. The very high temporal resolution allows for accurate direct modelling of unsteady non-periodic and turbulent flow at high Reynolds numbers with small time scales. For closer examination of the pulsatile flow fields, an additional simulation is performed with a high spatiotemporal resolution of 80 μm and 2.4 μs per numerical timestep and is also presented in § 3. This higher-resolution simulation is used for quantitative comparison with the pulsatile flow experiments. The flow domain is discretized into a mesh of 4824 × 408 × 408

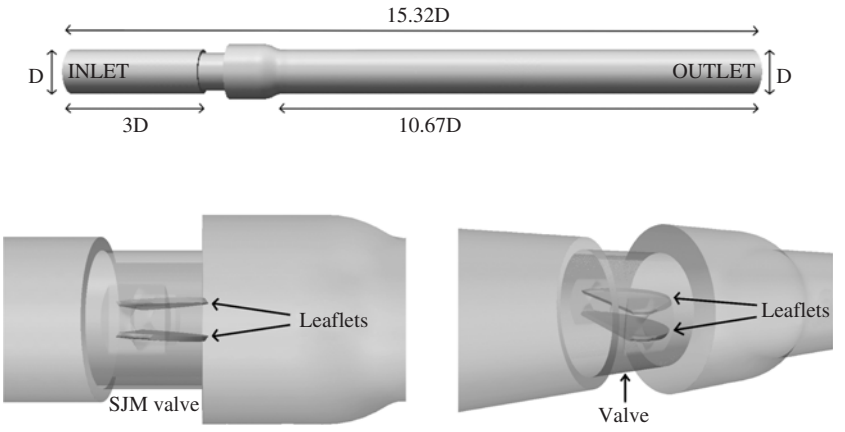

FIGURE 5. Computational model of the experimental *in vitro* flow loop.

grid nodes at this 80 μm spatial resolution for the axial and cross-sectional directions, respectively. An analysis on whether this spatial resolution captures the smallest Kolmogorov scales in pulsatile BMHV flows is made in § 4.3. Although the fluid domain employs uniform 3D grid spacing with no near-wall clustering, the resolution of the simulations is sufficiently high to accurately resolve the solid boundaries for both the valve housing and the leaflets.

The solid domain is created using Gambit©software, where the microCT scan and recreation of the experimental set-up is imported. The internal surface of the flow loop and the leaflet surfaces are discretized using an unstructured triangular mesh, which is immersed into the 3D fluid domain. The solid domain employed variable spatial resolution meshing: the ventricular inlet and aortic outlet cylinder lengths employ 320 μm length grid spacing, the valve region employs variable grid spacing from 20 to 40 μm, and the leaflets employ grid spacing from 20 to 50 μm.

Blood is modelled computationally as an incompressible Newtonian fluid, with the same physical properties as the blood analogue solution that was used experimentally. This computational matching of blood kinematic viscosity was also deemed suitable when validating against experimental blood damage studies (Wu *et al.* 2011).

The Womersley number, a dimensionless number of pulsatile flow frequency in relation to viscosity, and the Reynolds number are defined as

$$Wn = \frac{D}{2}\sqrt{\frac{\omega}{\nu}} \tag{2.10}$$

$$Re = \frac{U_{avg}D}{\nu} \tag{2.11}$$

where ω is the angular frequency of the pulsatile flow, D is the inlet diameter, ν is the kinematic viscosity and U_{avg} is the average velocity at the inlet based on experimental flowrate data. At the inlet of the domain (ventricular side), a plug flow profile is prescribed based on the time-varying flowrate curve data from the experimental study for pulsatile flow (figure 4(*a*)). A plug flow profile is employed due to the high Womersley number ($Wn = 18$) for this pulsatile BMHV flow. The maximum Reynolds number at peak flow of the cardiac cycle based on the inlet

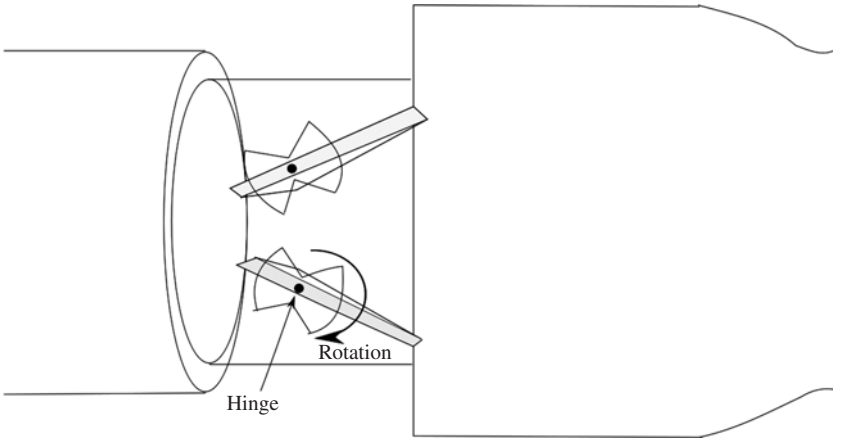

FIGURE 6. Demonstration of prescribed leaflet rotational motion about hinge fulcrum.

diameter is $Re = 5780$. For steady flow simulations, a fully-developed Poiseuille flow profile is prescribed at the ventricular inlet.

At the outlet of the domain (aortic side), a stress-free boundary condition is applied. This boundary condition is somewhat artificial when modelling higher-Reynolds-number flows, but necessary due to a finite length domain. In order to reduce its effects on the fluid flow in the region of interest, the outlet of the domain is extended in length before the stress-free boundary condition is applied on the aortic side. The flowrate inlet and stress-free outlet boundary conditions are applied as described for LBMs by Aidun *et al.* (1998).

Although pressure boundary conditions are not used in these simulations, it should be noted that in LBMs, pressure boundary conditions and velocity boundary conditions are similar in that they have the same effect of generating a fluid distribution function difference in the flow. Thus, the prescribed flowrate inlet and stress-free outlet boundary conditions act similar to pressure boundary conditions when used in LBMs. For details on pressure and velocity boundary condition implementation in LBM, refer to Zou & He (1996).

During the diastolic phase when the flowrate becomes negative, the inlet and outlet boundary conditions are switched, allowing two-way pulsatile flow. This allows the numerical method to accurately model the flow field during leaflet closing, leaflet-valve closing impact and diastolic reverse flow with fully closed leaflets. For diastole, the ventricular inlet length is observed to be sufficient so that the flow field is not affected by the presence of the stress-free condition on the ventricular side. No flow instabilities are found with this switching of boundary conditions to enable two-way flow. The high temporal resolution of the simulations results in near-zero flowrates when the boundary conditions are switched from forward to reverse flow (or vice versa), and thus flow instability issues at the inlet and outlet boundaries are not present.

Leaflet motion is prescribed throughout the cardiac cycle by prescribing the leaflet angle based on the experimental study results (figure 4*b*). The two leaflets of the BMHV design rotate about a hinge fulcrum line, with an angular sweep of approximately 55° for the SJM valve (see figure 6). This angular sweep is from 5 to 60°, with 0° referenced as parallel to the axial direction. The fulcrum line fixed at the hinges is parallel to the leaflet leading edge. The real SJM valve has tolerances with

the leaflet ear and hinge recess that allow for minimal translational motion along the parallel fulcrum axis. Although translational motion does occur in real SJM valves, the simulations of this study restrict leaflets to rotational motion only. No contact modelling is required and no singularity issues are found when the leaflets close against the valve housing. When the leaflets are fully open or fully closed, they are constrained in this position and no leaflet fluttering is modelled.

In these simulations, only one-way FSI is performed from the solid phase onto the fluid flow. This FSI is performed via the SBB method, where the motion of the leaflets imparts forces to the fluid phase via bounce-back links. As this study is performed for validation of the numerical method against experimental data, one-way FSI prescribing leaflet motion was deemed most suitable to match with experiments. The LBM is an explicit time-marching computational flow methodology, and although this might be an issue if the temporal resolution is low, the simulations of this study employ very high temporal resolution (2.4–4.8 μs per timestep). It is found in the pulsatile flow simulations that even with the explicit time-marching methodology, flowrates at cross-sections throughout the BMHV flow domain are consistently within 1 % of each other. This is found even in cases of high flowrate variation in the cardiac cycle, and thus there are no issues with flow 'lag' while using one-way FSI. Two-way FSI is possible with this numerical methodology, and will be briefly discussed in § 2.6.

Owing to the parallel computing capabilities of LBM, approximately 1000–3000 processor cores are used in parallel for all simulations with excellent scaling efficiency. The LB numerical method employed in this study has previously shown near perfect scaling efficiency up to 16 000 processor cores as demonstrated in Clausen, Reasor Jr & Aidun (2010). This scaling efficiency is performed with minimal FSI, and is thus considered optimal.

For the high 80 μm and 2.4 μs spatiotemporal resolution, one full cardiac cycle can be simulated in parallel with 2592 processors with a run time of less than 20 h. However, this corresponds to approximately 50 000 computational resource hours, and thus multiple cardiac cycles of simulation become very expensive. Thus, the pulsatile flow simulations of this study employ only one or two cardiac cycles for the highest spatiotemporal resolution due to computational resource constraints.

2.5. *Numerical–experimental comparison*

For initial validation of the LBM, axial velocity comparisons are made between the numerical simulations and experimental PIV data for steady flow past the fully open leaflets of a 23 mm SJM valve. This is performed with 160 μm spatial resolution for the numerical simulations. Quantitative comparisons are made for $Re = 750$ and 1250 for laminar flow, $Re = 2400$ representing the mid-acceleration phase and, finally, $Re = 5000$ representing the higher-Reynolds-number flows of the cardiac cycle with possible turbulent flow. For the experiments, an average flow field was computed over 100 time samples. For $Re = 750$ and 1250, due to the steady nature of laminar flows, only 1–5 computational time samples are needed for averaging for comparison with experiments. For $Re = 2400$ and 5000, due to the unstable nature of the higher-Reynolds-number flow, 200 experimental and computational time samples are used to determine an average flow field for comparison. The comparisons are made for axial velocity at perpendicular cross-section lines past the fully open leaflet trailing edges.

A mesh resolution comparison is also performed for the numerical simulations at varying spatial resolution. This is performed for steady flow at $Re = 5780$, representing

the peak flow Reynolds number of the cardiac cycle. A total 200 samples of numerical data are averaged for comparison between 160 and 80 μm spatial resolution. The mean flow fields for axial velocity are compared, as well as root-mean-square (r.m.s.) values for axial velocity.

For quantitative validation of pulsatile flow, simulations are performed for the cardiac cycle at 80 μm and 2.4 μs spatiotemporal resolution and comparisons are made with experiments at the high accelerating flow ($Re = 4700$), peak flow ($Re = 5780$) and decelerating flow ($Re \sim 1000$) timepoints. These quantitative comparisons are made for mean flow fields and r.m.s. values for axial velocity. These flow regimes are of interest for comparison due to high Reynolds number (accelerating and peak flow) and potential turbulence (peak and decelerating flow). Ideally, the quantitative comparison would be performed with numerical samples taken at these flow regimes and 200 cardiac cycles being simulated to match the experimental methods. However, this would result in a cost of approximately 10 million computational hours, which is beyond available resources.

As an alternative, 200 numerical samples are taken from the pulsatile flow simulations within one cardiac cycle. These samples are taken within a time range, centred about the flow timepoints of interest. The time range of numerical sampling is the integral time scale, also known as the turnover time of the largest eddies of the flow. The integral time scale, τ_0, is approximated from the Kolmogorov small eddy time scales as

$$\tau_0 = \tau_\eta \cdot Re^{1/2}. \tag{2.12}$$

For peak flow, this is calculated as $\tau_0 = 58.7$ ms, based on $Re = 5780$ and $\tau_\eta = 772$ μs (as determined in § 4.3). This is a simplification as compared with modelling 200 separate cardiac cycles to determine averaged flow fields as in experiments, but necessary due to resource limitations. However, the numerical samples are still taken within the integral time scale, where the largest and most significant flow structures would still be captured.

For accelerating and decelerating flow, the numerical time averaging is centred about the desired timepoint of comparison and the flowrate variation is close to linear within the integral time range. Thus, no flowrate normalization is required for comparison with experimental data as the averaged flowrate of the numerical samples is equivalent to the flowrate of the comparison timepoint. It is noted that the decelerating flow phase shows high variability from cycle-to-cycle in experiments such that Reynolds number is approximated ($Re \sim 1000$). Although this flow regime is of interest, good matching of simulations with experiments is not expected due to these cycle-to-cycle variations.

For peak flow, it is noted that there are cycle-to-cycle variations in the flowrate curves in the experiments, and thus the experimental sampling of the peak flow timepoint may not truly be capturing peak flow at every cardiac cycle. Thus averaging of 200 cardiac cycles of experimental data may similarly capture timepoints within the integral time range of peak flow, as is performed with numerical data. Once again, flowrate normalization is not required for this peak flow case.

It should also be noted that the use of 200 cardiac cycles in experiments is required due to cycle-to-cycle variation in leaflet motion and flowrates. The numerical simulations employ averaged leaflet motion and flowrate curves, thus prescribing 200 cardiac cycle averaged leaflet motion and flowrate from the experiments. The sampling of 200 numerical timepoints from one cardiac cycle of averaged experimental

conditions can be considered time averaging of flow data from an 'average' cardiac cycle. Mean flow fields at peak flow are compared using the same time sampling method for two different numerical cardiac cycles. Good comparison between the two cardiac cycles will demonstrate the appropriateness of the numerical sampling methodology.

For comparison of instantaneous features of pulsatile flow for the cardiac cycle, a qualitative comparison between the simulations and experimental data is performed. The comparisons are performed at key points of the cardiac cycle, namely: the opening phase (leaflets beginning to open at onset of systole), the acceleration phase (leaflets fully open with increasing flowrate), peak flow (leaflets fully open with maximum flowrate), deceleration phase (leaflets fully open with decreasing flowrate) and closing phase (sudden leaflet closing). Flow features, shown in the form of 2D out-of-plane vorticity contour plots, are compared downstream of the leaflets at instantaneous timepoints. Both the experiments and simulations employ the same contour scaling in all cases.

In summary, the numerical validation of LBM against experimental data will involve: quantitative comparison for steady flow at various Reynolds numbers, quantitative comparison for pulsatile flow and qualitative comparison of instantaneous pulsatile flow features, as well as numerical mesh resolution and data sampling comparison.

2.6. *FSI with the LBM*

The FSI in this study is enforced with the SBB method, which is capable of two-way FSI. The accuracy of two-way FSI with the SBB method has been documented extensively (Aidun & Lu 1995; Aidun *et al.* 1998; Macmeccan *et al.* 2008; Aidun & Clausen 2010) for the LBM. Two-way FSI with the leaflets of the BMHV is also possible for this numerical method.

A simulation is performed at 160 μm spatial resolution employing two-way FSI of the leaflets. Forces across the leaflet meshed surface are determined using the SBB method, and torques are accumulated for each leaflet based on calculated forces and the moment arm to the hinge fulcrum line. Allowing only for rotational motion about the hinge fulcrum line, the rotation of the leaflets is determined by solving Newtonian angular dynamics equations, with a moment of inertia of 4.375×10^{-9} kg m^2 for each leaflet. No hinge friction modelling is employed for this simulation, as this information is not known. The two-way FSI simulations are performed for a cardiac cycle after modelling an initial cardiac cycle with prescribed leaflet motion. This was performed to capture a more realistic starting flow field for two-way leaflet motion FSI with the remnants of the diastolic flow phase. Figure 7 shows the angle variation of the top and bottom leaflets from two-way FSI as compared with the experimental data.

For leaflet opening, the experimental data shows a 66.7 ms opening time from the fully closed to fully open leaflet positions. For the numerical simulations, the top leaflet opening time is 81 ms, and the bottom leaflet opening time is 64 ms. As flow inlet conditions and solid domain geometry are perfectly symmetric in the simulations, this shows natural asymmetry in leaflet motion due to the disorganized nature of the pulsatile BMHV flow field. Although there is noted asymmetry in leaflet opening, the leaflets are fully open at relatively close times in the cardiac cycle. The asymmetry in leaflet motion was also noted in the experimental study (Dasi *et al.* 2007).

For leaflet closing, the experimental PIV data shows a 40 ms closing time from the fully open to fully closed leaflet positions. For two-way FSI modelling, the top leaflet

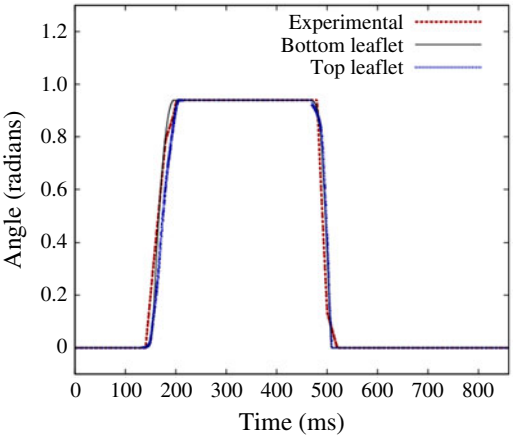

FIGURE 7. Angle variation from two-way FSI simulations as compared with experimental data.

closing time is 39 ms, and the bottom leaflet closing time is 38.5 ms. The ventricular side must be extended in length for two-way FSI simulations, causing a slight offset in the leaflet motion timing. Nevertheless, the leaflet motion time periods show very good comparison from simulations to experimental data when the leaflet motion start times are matched, as shown in figure 7.

Although two-way FSI with LBMs are possible and can even be employed in these BMHV flow simulations, the computational flow results of this study use only one-way FSI with prescribed leaflet motion. For best comparison of the flow fields, the conditions of the experiments must be matched as closely as possible. One-way FSI with prescribed leaflet motion ensures the best matching of conditions between simulations and experiments and is more reliable than using two-way FSI modelling. Real leaflet motion includes aspects such as friction with the hinges and slight translational shifting motion, neither of which is included in the computational model. Thus, it is determined that one-way FSI modelling is most appropriate for this work.

3. Results

3.1. *Steady flow comparison*

Figure 8 shows axial velocity comparisons between the numerical simulations and the experimental data for laminar flow at $Re = 750$. This represents the early acceleration phase of the cardiac cycle. These velocity comparisons are taken at perpendicular (x–y) cutplanes taken at the tube centre ($z = 0$ mm). The numerical results agree very well with the experimental data, particularly for the bottom jets. The first plot is taken immediately downstream of the end tips of the leaflets ($x = 2.2$ mm). The slight asymmetry of the experimental results is apparent as the flow is stronger through the bottom jet than the top jet. The bottom jet shows excellent agreement between the numerical and experimental data. The remaining five plots, showing comparisons further downstream, indicate good matching between the numerical results and experimental data. The asymmetry of the experimental data is apparent in all of the experimental plots as the top jet is consistently weaker than the bottom jet. This lack of perfect symmetry in the experimental data was noted in the previous computational–experimental steady flow validation work as well (Ge

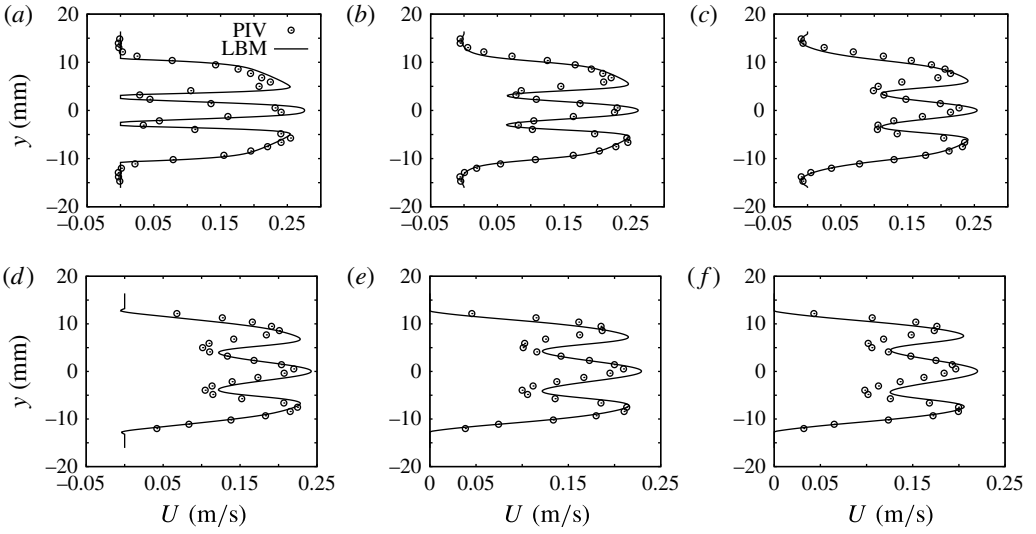

FIGURE 8. Steady flow comparison at $Re = 750$: (*a*) $x = 2.2$ mm; (*b*) $x = 10.3$ mm; (*c*) $x = 20.1$ mm; (*d*) $x = 30.9$ mm; (*e*) $x = 40.7$ mm; (*f*) $x = 50.6$ mm.

et al. 2005). Nevertheless, the middle jets and particularly the bottom jets show good numerical–experimental agreement for all plots.

Comparisons at $Re = 1250$ (figure 9) represent the early-to-mid acceleration phase of the cardiac cycle. As flow at $Re = 1250$ is still laminar in nature, only five computational time samples are averaged for comparison with experiments. The comparisons at this second laminar flow regime again show very good matching between simulations and PIV data. Once more, the slight asymmetry of the experimental results is demonstrated, as the bottom jet flow is consistently stronger than the top jet. This asymmetry of experimental data is demonstrated in all plots. The bottom jets show the best numerical-to-experimental agreement, with the middle jets showing good agreement as well. The simulations are also able to capture some negative axial velocities near the housing walls in the sinus expansion, representing recirculating flow.

Comparisons at $Re = 2400$ (figure 10) represent the mid-acceleration phase of the cardiac cycle, where some disorganized flow is present. Due to some unsteadiness in vortex shedding at this Reynolds number, 100 computational time samples are averaged for comparison with experiments. The plots show good comparison between the simulations and experiments at this representative mid-acceleration Reynolds number. The experimental results show the triple orifice jets to have slightly more blunted profiles than in the numerical results. Although the lateral jets match well between simulations and experiments, the slightly more blunted profiles near the peak values is not precisely matched by the simulations.

The central jet in the experiments is also consistently weaker than the lateral jets. This is in contrast to the simulations where the central jet is consistently stronger than the lateral jets. This trend is particularly noted 20.0 mm downstream of the leaflets. Nevertheless, all comparisons taken downstream of the leaflet tips show similar good agreement between simulations and experiments for the lateral jets. The negative axial velocities near the valve housing are again shown in both the experiments and simulations, representing the recirculation region in the aortic sinus expansion.

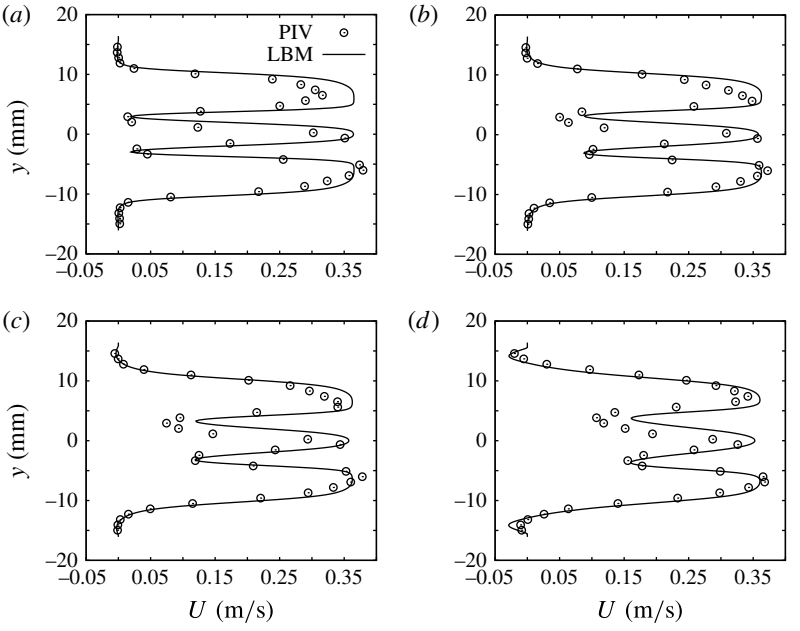

FIGURE 9. Steady flow comparison at $Re = 1250$: (*a*) $x = 2.2$ mm; (*b*) $x = 6.7$ mm; (*c*) $x = 10.2$ mm; (*d*) $x = 20.1$ mm.

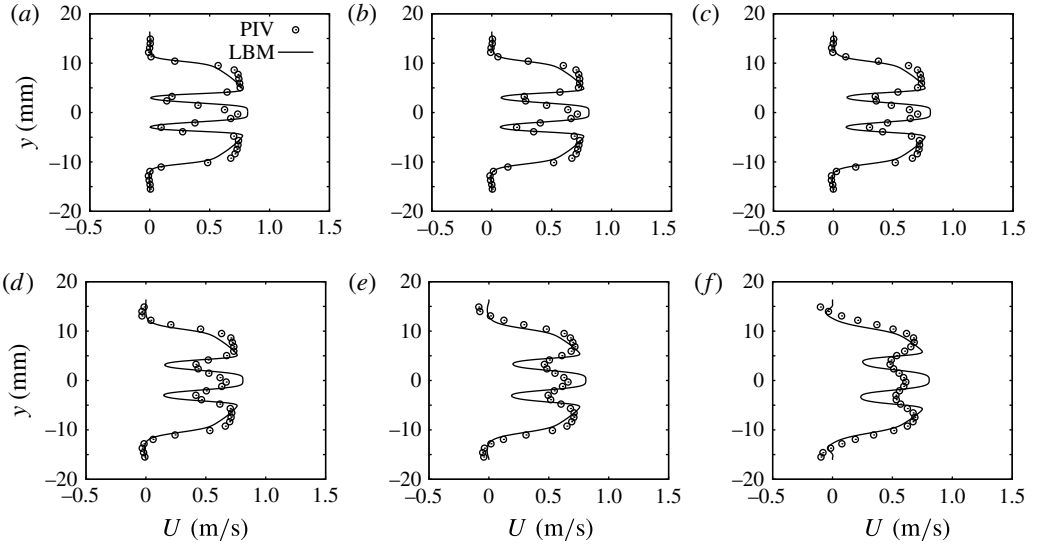

FIGURE 10. Steady flow comparison at $Re = 2400$: (*a*) $x = 3.1$ mm; (*b*) $x = 5.8$ mm; (*c*) $x = 7.5$ mm; (*d*) $x = 10.3$ mm; (*e*) $x = 13.8$ mm; (*f*) $x = 20.0$ mm.

Figure 11 shows axial velocity comparisons for flow at $Re = 5000$. Comparisons at this Reynolds number represent the near-peak-flow phase of the cardiac cycle, with highly disorganized and unstable flow structures. The plots show very good

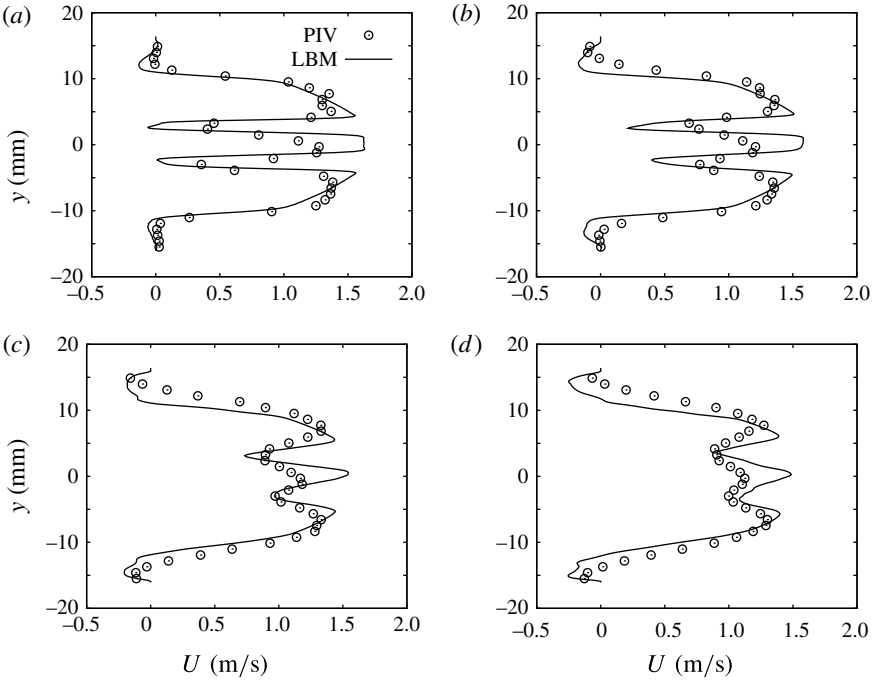

FIGURE 11. Steady flow comparison at $Re = 5000$: (*a*) $x = 3.1$ mm; (*b*) $x = 7.5$ mm; (*c*) $x = 13.8$ mm; (*d*) $x = 18.3$ mm.

comparison between simulations and experiments at this representative peak-flow Reynolds number. Both the experiments and numerical simulations show blunted profiles for the three orifice jets. For the lateral jets, the simulations slightly overshoot the peak velocities compared with experiments, but still match well. The highly disorganized flow at this Reynolds number is apparent from these comparisons as well, as the flow profiles are not symmetric even with averaging over 200 computational and experimental samples. This is in contrast to lower-Reynolds-number cases that show symmetric flow profiles for simulations when averaging over sufficient time samples.

Like the $Re = 2400$ case, the central jet is consistently weaker than the lateral jets for the experiments. For the simulations at $Re = 5000$, the central jet is of the same strength when compared with the lateral jets. All comparisons show very good agreement between simulations and experiments for the lateral jets. The negative axial velocities near the valve housing are highlighted in the simulation results, which show strong reverse velocities in the sinus expansion region.

The comparison locations and maximum mean flow axial velocities at these locations are summarized for steady flow experiments and simulations at various Reynolds numbers in table 1. Not all comparison points are listed, but one comparison location close to the leaflets and one farther downstream are listed for all Reynolds numbers. For higher Reynolds numbers ($Re = 2400$ and $Re = 5000$), the maximum velocity values do not match as well as for lower Reynolds numbers. Comments are made about the central jet matching for $Re = 2400$ and 5000 in § 4.

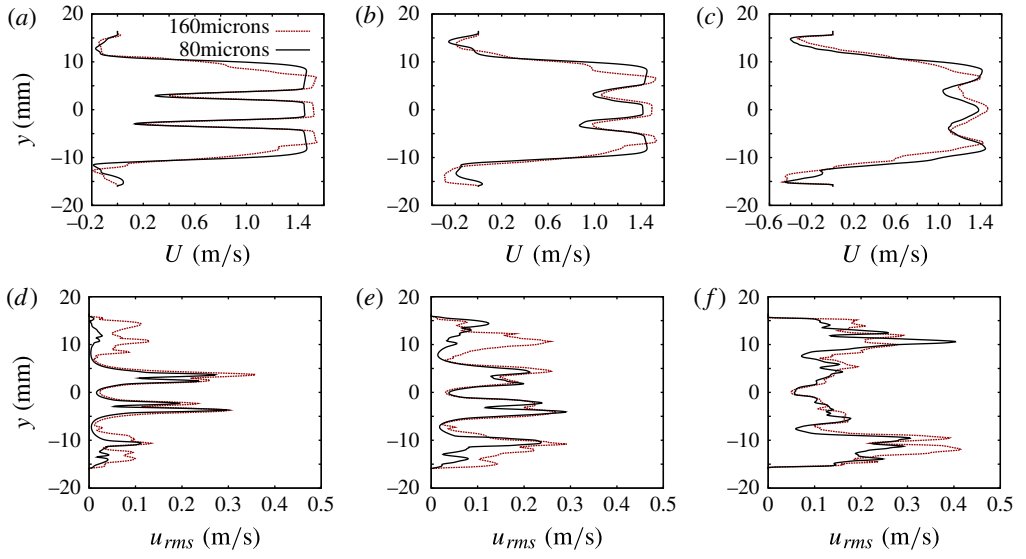

FIGURE 12. (Colour online) Comparison of mean axial flow (*a–c*) and r.m.s. (*d–f*) velocity values at steady peak flow ($Re = 5780$) for numerical simulations at varying fluid spatial resolution: (*a*) $x = 5.0$ mm; (*b*) $x = 10.1$ mm; (*c*) $x = 20.1$ mm; (*d*) $x = 5.0$ mm; (*e*) $x = 10.1$ mm; (*f*) $x = 20.1$ mm.

Re	Distance from leaflet (mm)	Max U_{avg} (experiment) (m s^{-1})	Max U_{avg} (LBM) (m s^{-1})
750	2.2	0.25	0.27
750	30.9	0.22	0.24
1250	2.2	0.38	0.36
1250	20.1	0.37	0.36
2400	3.1	0.75	0.81
2400	20.1	0.69	0.80
5000	3.1	1.4	1.62
5000	18.3	1.27	1.48

TABLE 1. Steady flow comparison.

3.2. *Numerical mesh resolution comparison*

Figure 12 shows comparison of mean axial flow velocities and r.m.s. values at perpendicular lines for numerically simulated flows resolved at 160 μm versus 80 μm. The numerical comparisons are performed at steady flow past the open leaflets with $Re = 5780$, representing the peak flow regime. Computational resource limitations prohibit the calculation of mean flow fields and r.m.s. data for 200 separate cardiac cycles of pulsatile flow through a BMHV, and thus a mesh comparison is performed for steady flow only.

Mean flow fields are computed by averaging 200 computational time samples. The mean flow results (figure 12*a–c*) taken downstream of the trailing leaflet tips show that the peak orifice velocities at 160 μm resolution are slightly higher with sharper flow profiles when compared with the flow resolved at 80 μm. Although the 80 μm flow

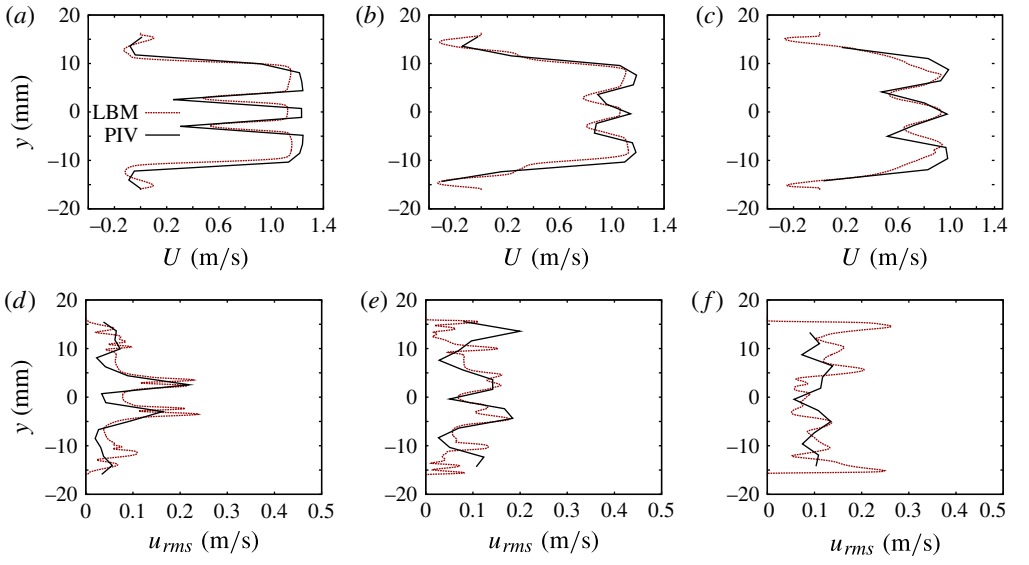

FIGURE 13. (Colour online) Comparison of mean axial flow (*a–c*) and r.m.s. (*d–f*) velocity values at accelerating flow ($Re = 4700$) for simulations against experiments for pulsatile flow: (*a*) $x = 5.0$ mm; (*b*) $x = 10.1$ mm; (*c*) $x = 20.0$ mm; (*d*) $x = 5.0$ mm; (*e*) $x = 10.1$ mm; (*f*) $x = 20.0$ mm.

profiles are smoother, the overall flowrate at the perpendicular lines are very similar for both spatial resolutions. The mean flow fields, though showing some differences at the flow peaks, are still very similar and well captured at the coarser 160 μm resolution.

Figure 12(*d–f*) shows axial velocity r.m.s. values taken at the same perpendicular lines. For the central flow emerging from the valve, the comparison of r.m.s. values is excellent from 160 to 80 μm. The largest discrepancies are found outside the central region, representing the sudden sinus expansion region. This difference could be explained by the disorganized nature of flow within this expansion recirculation region, and also by the 160 μm case interpolating a sharper expansion step due to coarser resolution of the FSI boundary. Nevertheless, the central orifice r.m.s. comparison shows very good agreement.

Combined with the good agreement for mean flow fields, this justifies the 160 μm resolution simulation as suitable for comparison against PIV experimental data for mean steady flow and pulsatile bulk flow features. However, for quantitative comparison of pulsatile flow and finer details in pulsatile flow visualization, and for highly accurate flow simulations, 80 μm resolution simulations are desirable.

3.3. *Pulsatile flow quantitative comparison*

Quantitative comparisons of pulsatile flow are shown in figures 13–15 for three representative flow regimes. The high-resolution simulations (80 μm and 2.4 μs) take 200 samples for each flow regime but only from one cardiac cycle, and are compared with 200 cardiac cycle ensembles from the experiments. The three flow regimes, high accelerating flow ($Re = 4700$), peak Reynolds number flow ($Re = 5780$) and decelerating flow ($Re \sim 1000$), demonstrate the most unstable and possibly

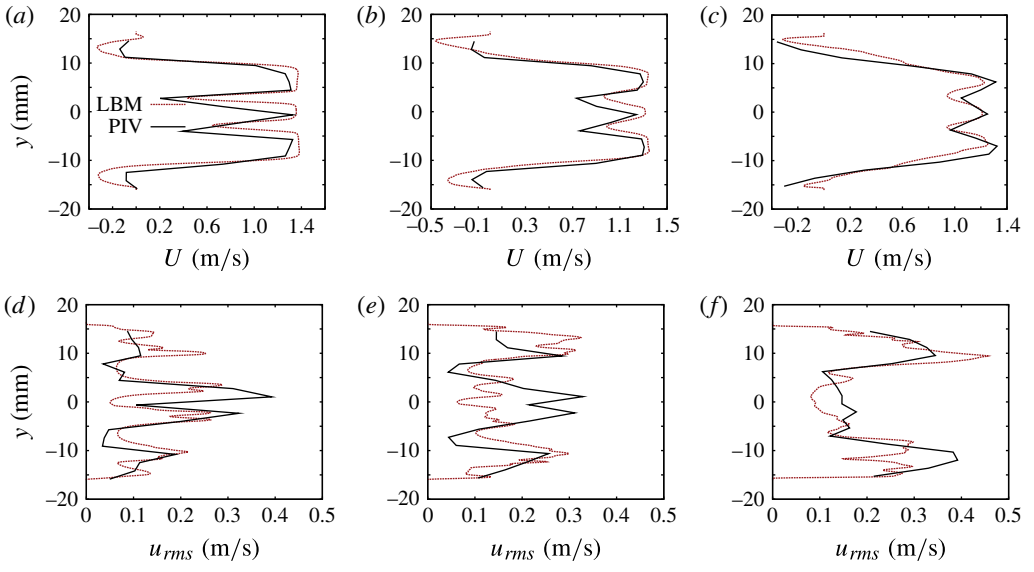

FIGURE 14. (Colour online) Comparison of mean axial flow (*a–c*) and r.m.s. (*d–f*) velocity values at peak flow ($Re = 5780$) for simulations against experiments for pulsatile flow: (*a*) $x = 5.0$ mm; (*b*) $x = 10.1$ mm; (*c*) $x = 20.0$ mm; (*d*) $x = 5.0$ mm; (*e*) $x = 10.1$ mm; (*f*) $x = 20.0$ mm.

turbulent flow. Thus quantitative comparison is performed by computing mean flow fields and r.m.s. data. A total of 200 numerical samples are used to match the number of experimental samples taken for averaging flow fields. However, it is determined that even 50 numerical samples are sufficient to determine mean flow fields, and thus 200 samples are used to obtain improved r.m.s. data.

Figure 13 shows comparisons at the high accelerating flow phase ($Re = 4700$). This flow regime is considered transitional, if not turbulent, flow. Mean flow field comparisons at three axial locations show good matching between simulations and experiments. Both simulations and experiments also capture negative axial velocities at the sinus expansion regions, although the simulations show larger negative velocities. The simulations also show smoother profiles than experiments, which could be due to the higher resolution of the numerical data in comparison with the experiments. Overall, the simulations and experiments match very well.

The r.m.s. data also shows good matching, particularly at 5.0 mm downstream of the leaflet tips. The biggest mismatch at all comparison points lies in the sinus expansion regions, which can be explained by the disorganized mixing that occurs in this region. At 20.0 mm downstream of the leaflets, this difference is more apparent, but it should be noted that the experimental r.m.s. data is cut off near the sinus expansion. Overall, the r.m.s. data shows good matching between simulations and experiments.

At peak flow (figure 14), the numerical simulations and experiments compare very well for mean flow fields at various distances from the leaflet tips. The experimental profiles are slightly lower in magnitude and have sharper orifice flow profiles. The sharper profiles may be attributed to the experimental data resolution being coarser than the numerical simulations. Nevertheless, the comparison still shows very good agreement even at peak Reynolds number.

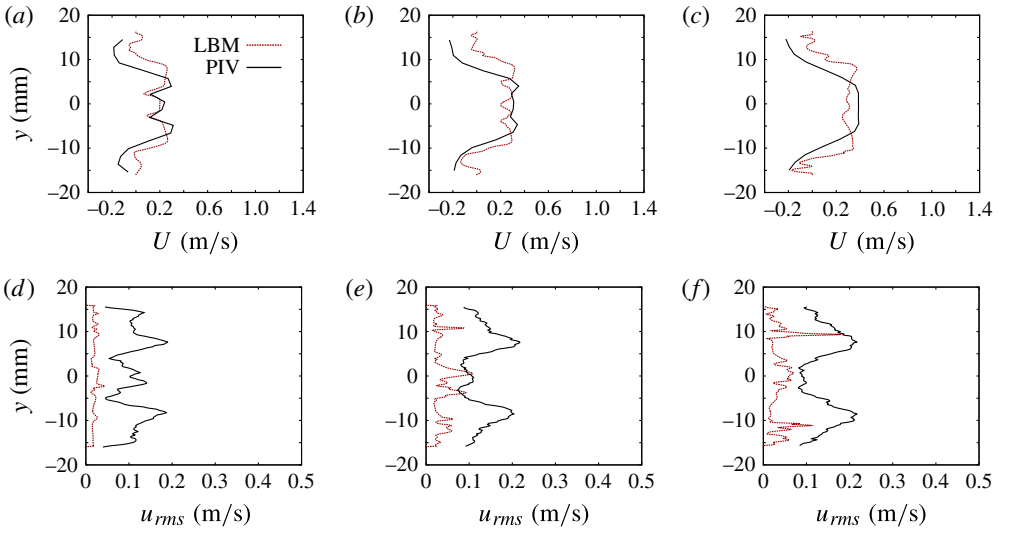

FIGURE 15. (Colour online) Comparison of mean axial flow (*a–c*) and r.m.s. (*d–f*) velocity values at decelerating flow ($Re \sim 1000$) for simulations against experiments for pulsatile flow. (*a*) $x = 5.0$ mm. (*b*) $x = 10.1$ mm. (*c*) $x = 20.0$ mm. (*d*) $x = 5.0$ mm. (*e*) $x = 10.1$ mm. (*f*) $x = 20.0$ mm.

Quantitative comparisons are also made for the deceleration phase of the cardiac cycle (figure 15), which is a highly disorganized and unstable flow period. The deceleration phase Reynolds number is approximated at $Re \sim 1000$, although this may vary highly from cycle to cycle. The mean flow fields show similar velocity magnitudes and overall flowrates at perpendicular lines past the leaflet tips, but the matching of velocity profile is not as good as in the comparison of the accelerating and peak flow phases. The experimental data show more blunted profiles, likely due to coarser resolution and flow averaging across highly varying cardiac cycles. The experimental data also show lower velocity magnitudes further from the centre of the cross-section, at each perpendicular line. Although the mean flow comparison between simulations and experiments is not very good at this deceleration phase, the overall flowrates are similar. It is emphasized that the deceleration phase is very unstable and varies highly from cycle to cycle in the experiments, and thus good matching with simulations is not expected.

The r.m.s. data comparison shows that experimental r.m.s. values are consistently much higher than the numerical simulations. This r.m.s. data comparison again demonstrates the high variation in experiments from cycle-to-cycle in the deceleration phase, once again showing the difficulty of comparison between simulations and experiments at this representative flow regime.

Further comments on the quantitative pulsatile flow matching between simulations and experiments will be made in § 4. The comparison locations and maximum mean flow axial velocities at these locations are summarized for accelerating flow, peak flow, and decelerating flow in table 2. The PIV data and simulations compare well for these maximum axial velocity values, even for these complex and unstable flows.

The same numerical averaging method of using 200 time samples within one cardiac cycle is used for a second modelled cardiac cycle. The comparison of mean flow fields for these two separate cardiac cycles is given in figure 16. Although the mean

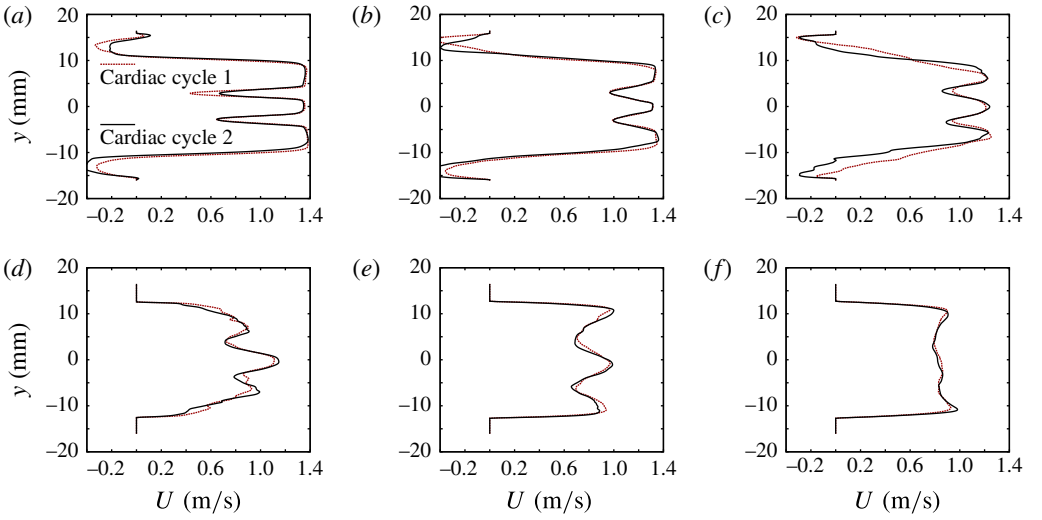

FIGURE 16. (Colour online) Comparison of mean axial velocity values at peak flow ($Re = 5780$) for simulations at two different cardiac cycles: (*a*) $x = 5.0$ mm; (*b*) $x = 10.1$ mm; (*c*) $x = 20.0$ mm; (*d*) $x = 30.0$ mm; (*e*) $x = 50.0$ mm; (*f*) $x = 70.0$ mm.

Flow regime	*Re*	Distance from leaflet (mm)	Max U_{avg} (experiment) (m s^{-1})	Max U_{avg} (LBM) (m s^{-1})
High acceleration	4700	5.0	1.24	1.16
High acceleration	4700	10.1	1.19	1.13
High acceleration	4700	20.0	0.97	0.89
Peak	5780	5.0	1.31	1.38
Peak	5780	10.1	1.31	1.35
Peak	5780	20.0	1.30	1.25
Deceleration	1000	5.0	0.27	0.30
Deceleration	1000	10.1	0.32	0.34
Deceleration	1000	20.0	0.37	0.39

TABLE 2. Pulsatile flow comparison.

flow fields are taken from two cardiac cycles, flowrate and leaflet motion conditions are identically prescribed as 'averaged' experimental conditions. The comparison of mean flow fields between the two cardiac cycles is very good, matching well as far as 70 mm downstream of the leaflet tips. For 5 and 10 mm downstream of the leaflet, the comparison is excellent. This good matching between two cardiac cycles demonstrates the appropriateness of the numerical time averaging from one cardiac cycle. This shows that the computational method is able to model an 'average' cardiac cycle repeatably, using average flowrate and leaflet motion data from 200 experimental cardiac cycles.

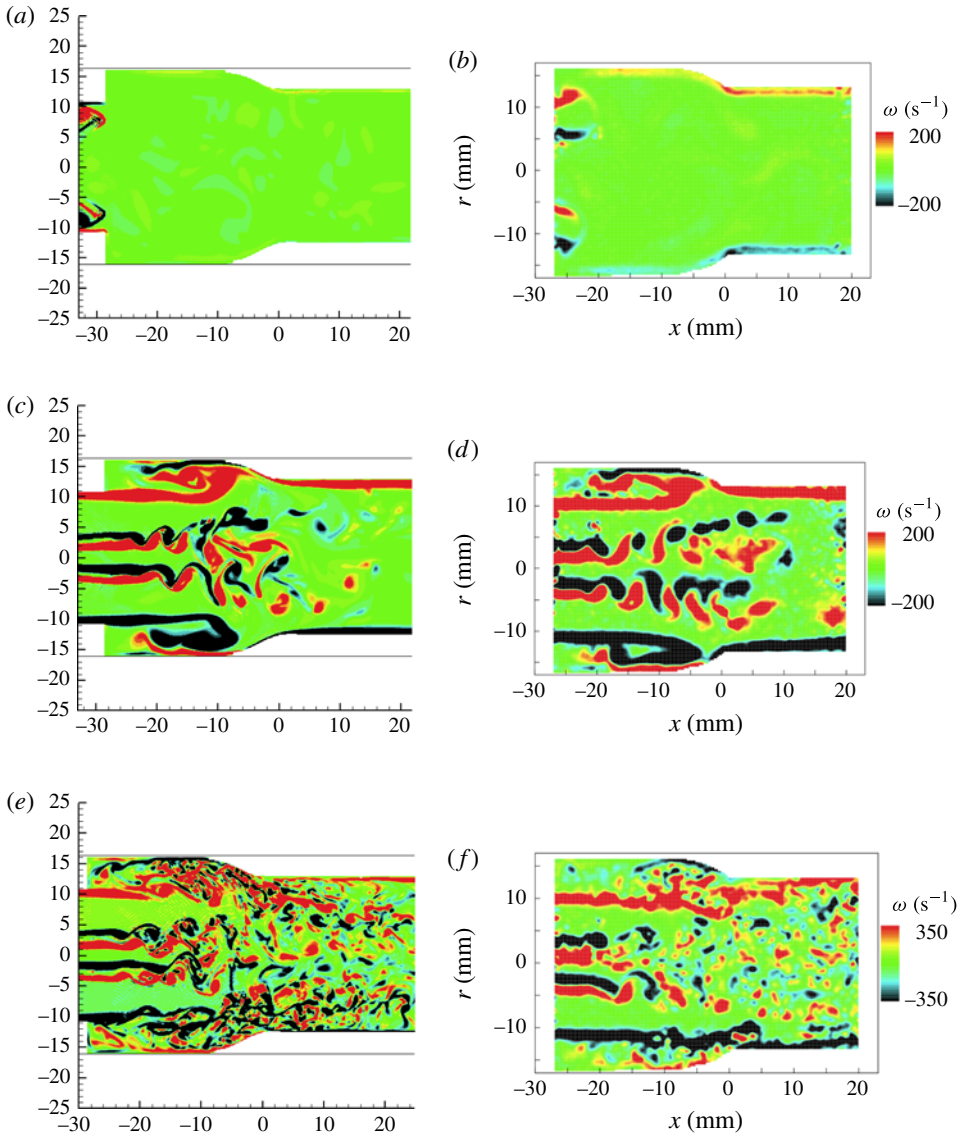

FIGURE 17. 2D vorticity magnitude comparison between simulation and experiments for pulsatile BMHV flow at opening, acceleration and peak flow phases: (*a*) opening, computational; (*b*) opening, experimental; (*c*) acceleration, computational; (*d*) acceleration, experimental; (*e*) peak, computational; (*f*) peak, experimental.

3.4. *Pulsatile flow qualitative comparison*

For qualitative validation of pulsatile flow, comparisons are made at instantaneous time points throughout the cardiac cycle. This is because ensemble averaging of experimental data removes some key flow features that are important for instantaneous time comparison. In all comparisons, the same vorticity scaling is employed for both experiments and simulations. Figure 17(*a*,*b*) shows instantaneous out-of-plane vorticity magnitude at the opening phase of the cardiac cycle ($Re = 240$), which is characterized

by two notable features. One shear layer exists from separation of flow at the edge of the valve housing to the sudden sinus expansion region, and another exists from flow separation at the tip of the leaflets as they suddenly open. These are opposite in magnitude and good qualitative comparison is shown with the experiments for both of these features. Figure 17(*c*,*d*) shows the accelerating phase ($Re = 2070$) where the leaflets are fully open and the flow rate past the valve increases. Here the flow past the leaflet tips causes two coherent von Karman vortex wakes. In addition, recirculation vortices are seen in the sinus aortic expansion region. The numerical simulations and experiments match very well qualitatively during this phase of the cardiac cycle.

Figure 17(*e*,*f*) is at peak flow, with a Reynolds number of 5780. The same qualitative flow features of vortex shedding wakes and recirculation vortices from the acceleration phase are shown in this peak flow phase, but with more unstable motion due to the higher Reynolds number. Although it appears that there are still two vortex shedding wakes from flow past the leaflet tips, this becomes highly disorganized and breaks apart quickly downstream of the valve in the sinus expansion. The shear layer from the sinus step also results in a recirculation region in the sinus expansion, but is broken into smaller scale structures. Downstream, the coherent structures completely break apart into small-scale vortices, which eventually wash out due to viscous dissipation. Qualitatively, the simulations and experiments agree well at this high-Reynolds-number flow regime.

Figure 18(*a*,*b*) shows the deceleration phase ($Re \sim 1000$), with the leaflets still fully open, but with a rapidly decelerating flowrate. The decelerating flow leads to a breakup of the coherent vortical structures downstream of the valve, shown in both the simulations and experiments. The shear layer from the valve housing into the sinus expansion still exists, but no longer develops into a significant recirculation region. Although the vortex shedding past the leaflet tips still exists, it does not form coherent vortex streets, instead immediately breaking down into smaller eddies. Downstream of the sinus region, only small-scale structures exist that are rapidly dissipated. The experimental results show more viscous dissipation than the numerical results downstream of the sinus region but the two still compare well.

Figure 18(*c*,*d*) is a final timepoint at the closing phase ($Re = 580$ in reverse direction flow), where the leaflets slam shut due to an adverse pressure gradient. Here, the sudden leaflet closing motion results in vortex wakes that are seen in both the simulations and experiments. The downstream flow is primarily characterized by smaller scale structures that are dissipating rapidly due to the lower flowrate and viscous dissipation.

4. Discussion

4.1. *Comparison with experiments*

A primary concern exists as to whether the LBM is appropriate for modelling BMHV flows. For experimental validation, the pulsatile PIV data averaged flow features due to cycle-to-cycle variability and lower spatial resolution. Despite these limitations, the experimental data is enough to delineate the key bulk flow features of pulsatile BMHV flow, but would average out the turbulent Kolmogorov scales. Thus, for qualitative comparison of bulk flow features with the pulsatile experimental data, the 160 μm resolution of the computational simulations is sufficient. For steady flow, comparison at $Re = 750$ does not require a high spatial resolution due to the flow being in the laminar regime. For steady flow at $Re = 2400$ and 5000, the comparison

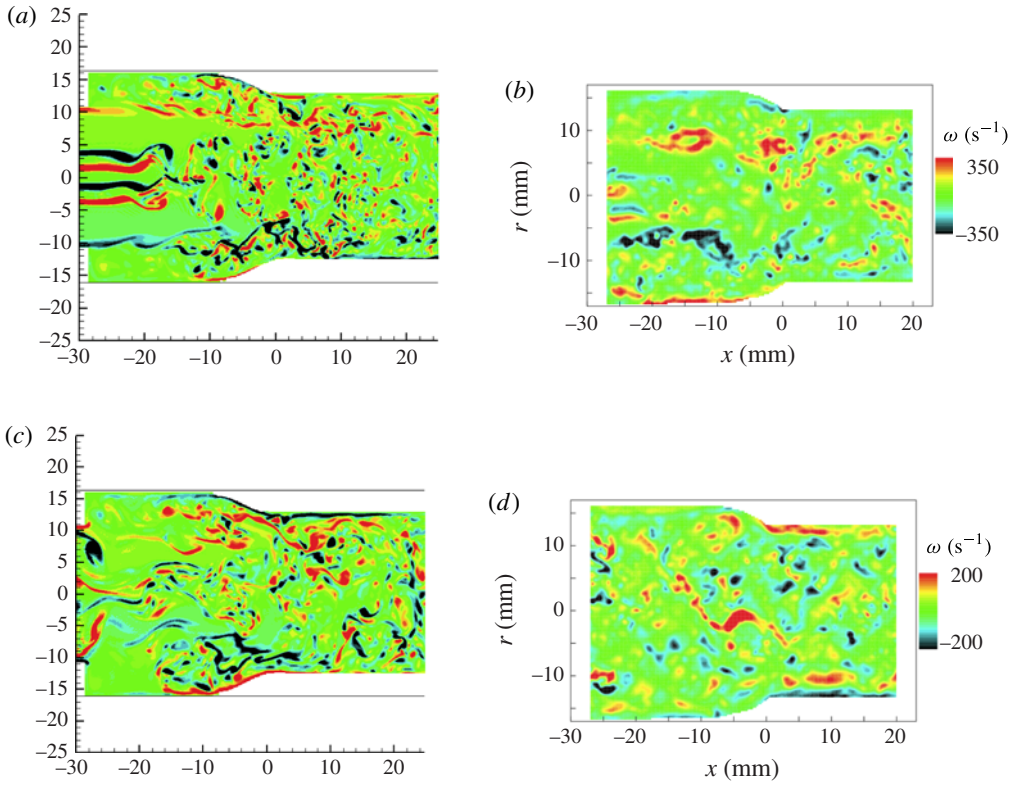

FIGURE 18. 2D vorticity magnitude comparison between simulation and experiments for pulsatile BMHV flow at deceleration and closing phases: (*a*) deceleration, computational; (*b*) deceleration, experimental; (*c*) closing, computational; (*d*) closing, experimental.

is made for mean flow with an average of 100–200 time samples for both the experiments and simulations, making the Kolmogorov turbulent fluctuation scales irrelevant in this steady flow comparison. Thus, the turbulent Kolmogorov scales are not important for all cases of steady flow comparison as well as for qualitative pulsatile flow comparison. The comparison between 80 and 160 μm resolution shown in figure 12 also demonstrates that the mean flow fields are sufficiently captured at coarser 160 μm resolution for use in experimental comparisons in these cases.

The numerical-to-experimental comparison was performed to prove the validity of LBM for use in modelling BMHV flows. For quantitative comparison, cases of steady flow past the fully open leaflets are used. This was chosen as a more reliable way to compare simulations with experiments quantitatively without having the issues of cycle-to-cycle variability that exists in pulsatile flow experiments. When comparing in the laminar regimes of $Re = 750$ and 1250 (figures 8 and 9), it is noted that the LBM compares very well with the experimental PIV data. Even as far downstream as 50.6 mm past the leaflet tips, the numerical simulations match the flow profile and velocity magnitudes of the triple jet flow structure well. It is noted in the previous work (Ge *et al.* 2005) and from the comparison in this study that a natural asymmetry of the top and bottom orifice flows exists in the experimental data due to design imperfections. Owing to the perfect top–bottom symmetry in the computational model, this asymmetry is not present in the numerical results. Despite this, the numerical

results show good quantitative agreement with the experiments, particularly in the central and bottom orifice flows.

For $Re = 2400$ and 5000 (figures 10 and 11), the LBM compares well in the lateral jets but not as well in matching the central jet. In all cases, the numerical simulations overshoot the peak velocities of the triple orifice flow structure. For the previous study of numerical-to-experimental quantitative comparison at $Re = 5000$ (Ge *et al.* 2005), the simulations of a different numerical method were also shown to consistently overshoot the peak velocities of the triple flow jets as well as show sharper jet profiles. It is possible that the experimental data show a more blunted profile with lower peak velocities due to the averaging of the instantaneous realizations of flow. Even though the flow is steady, at higher Reynolds number there are smaller features that vary between instantaneous time samples of experimental data which are lost due to ensemble averaging, resulting in a more blunted profile.

The central jet in the simulations is consistently stronger than the lateral jets at all comparison points, which is opposite of the experimental results. It is noted in the experiments that the maximum flow velocity does occur in the central orifice jet, as expected due to the minimal orifice area. However, in the experiments, this maximum velocity value is found within the valve in the axial location between the leading and trailing leaflet edges. The experimental data comparison points, however, are downstream of the leaflet tips, where the lateral jet velocities become stronger than the central orifice jet velocities. A possible reason for this inconsistency may be due to the computational recreation of the leaflets. The leaflets in the simulations were created by scaling down the original microCT scanned leaflet geometry. This was performed due to the constraints of a numerical method used in a previous study. In addition, the leading edge tips of the leaflet were slightly cut off during scanning. These modifications to the original geometry led to a slight increase in the central orifice area. However, the increased central orifice area was within the range given by SJM valve standards and did not affect the bulk flow. Although this modified leaflet geometry and increased b-datum area do not affect the overall results of this study, it can explain why the simulations show consistently stronger central orifice jets downstream of the trailing leaflet edges.

For comparison between 160 and 80 μm resolution simulations at steady $Re = 5780$ flow, the mean flow fields show good agreement. The slightly sharper profiles at 160 μm can be attributed to the coarser resolution. In addition, the coarser resolution of the FSI boundary at the valve surfaces could lead to the sharper profile for the lateral jets at 160 μm. For r.m.s. comparison, the central orifice values compare very well, with the major differences located in the sinus expansion region. The nature of the recirculating flow in the sinus region at peak Reynolds number is very unstable and disorganized, and thus some discrepancy can be expected. In addition, the coarser resolution would once again interpret the sudden sinus expansion step differently between 160 and 80 μm. Despite these differences, the mean flow and r.m.s. values between the two resolutions show good agreement, and thus validate the 160 μm case for comparison against experimental data. Bulk flow features are well-captured at 160 μm, which is key for experimental comparison. However, for the finest details of this pulsatile BMHV flow, future simulations should use the higher resolution at 80 μm.

Quantitative comparisons of mean flow fields and r.m.s. values are also made for pulsatile flow at three flow regimes, using the higher 80 μm numerical simulations (figures 13–15). For the mean flow fields at accelerating and peak flow (figures 13 and 14), the experimental data show sharper profiles in axial velocities for both flow

regimes. The sharper flow profile of the experimental data can be attributed to the lower PIV data resolution. For peak flow (figure 14), the experimental data show slightly lower axial velocity magnitudes in each comparison. However, it is noted that the experimental data is taken from 200 cardiac cycles of pulsatile flow. As there are cycle-to-cycle variations in the experiments, it is likely that the PIV system is unable to exactly capture peak flow timepoints for every cardiac cycle ensemble. Thus, as peak flow cannot be exactly captured consistently, the overall mean flow velocities are expected to be lower in magnitude for the experiments. Nonetheless, it is noted that the mean flow fields still match well from simulations to experiments for all comparison points at the accelerating and peak flow regimes. At decelerating flow (figure 15), the overall flowrates are matched between simulations and experiments, but the flow profiles do not match very well due to high cycle-to-cycle variations of the deceleration flow phase. This may also explain the more blunted velocity profiles for mean flow fields in the experiments for decelerating flow.

For r.m.s. values at accelerating and peak flow (figures 13 and 14), the comparison between experiments and simulations generally matches well. A primary difference in r.m.s. values is noted at peak and decelerating flow (figures 14 and 15) in the higher magnitude of r.m.s. peak values in experiments compared with simulations. These r.m.s. values for experiments and simulations include fluctuations due to the disorganized and unstable nature of the peak and decelerating flow regimes. However, the experimental data also have fluctuations due to strong cycle-to-cycle variations in the flow field. These cycle-to-cycle fluctuations are not present in the r.m.s. values of the simulations due to the numerical time averaging from within one cardiac cycle. Thus, the overall r.m.s. values for experimental data are increased, which can explain the higher peak r.m.s. values for experiments as compared with the simulations. This is particularly apparent at the deceleration flow phase where cycle-to-cycle variability results in much higher r.m.s. values for the experiments.

A limitation of the numerical simulations is that 200 cardiac cycles cannot be simulated due to resource limitations. Ideally, quantitative comparison for pulsatile flow would include the modelling of many cardiac cycles in order to more accurately compare mean flow fields and r.m.s. values as is performed experimentally. The numerical simulations are performed for pulsatile flow, but the data samples are taken from one cardiac cycle. This is time averaging and not ensemble averaging, but the numerical data samples are taken within a time range corresponding to the integral time scale for each Reynolds number. This should capture the major flow structures for each flow regime that is compared. The noted cycle-to-cycle variability in experiments could similarly lead to experimental data samples taken within this time range for pulsatile flow. In addition, the 200 cardiac cycles are necessary for experiments to average leaflet motion and flowrate cycle-to-cycle variation. Numerically, this variation does not exist as the averaged flowrate and leaflet motion is prescribed exactly. Thus, the numerical method of attaining 200 time samples of pulsatile flow is a viable alternative for comparison to experiments, and also shows good matching with experiments in figures 13–15. In addition, the comparison of mean flow fields between two cardiac cycles using the same numerical sampling method (figure 16) shows very good matching, further demonstrating its applicability.

Although cycle-to-cycle variations exist in pulsatile flow through the SJM valve, good qualitative agreement is observed when comparing simulations to experiments at multiple instantaneous timepoints throughout the cardiac cycle. The LBM is able to match key flow features very well, particularly during the opening and acceleration

phases of the cardiac cycle (figure 17). During these two time points, the flow is still highly organized and experimental data show clear features such as von Karman vortex streets or sinus recirculation regions, which are also reproduced numerically. The vortex shedding in accelerating flow is still in the laminar regime and repeatable from cycle to cycle.

During the more chaotic peak flow and deceleration flow phases (figures 17 and 18), these features become highly disorganized and it is difficult to pick out clear features in the experimental data. Cycle-to-cycle variability is also more prevalent in these flow phases. Although the vortex streets and recirculation regions are present, they are not clearly discernible in either the simulations or experiments and thus it becomes difficult to show a clear matching. The deceleration and closing phases are also characterized by high dissipation of vorticity and turbulent mixing, which also makes comparison difficult. However, in the closing phase (figure 18), the key feature of vortex wakes caused by rapid leaflet closing compares well between simulations and experiments. The overall good quantitative and qualitative agreement of numerical simulations with experiments validates the use of LBM for modelling various cases of pulsatile flows through BMHVs.

4.2. *Higher-resolution modelling and lattice-Boltzmann advantages*

Figure 19 shows out-of-plane vorticity contours for two timepoints of systolic flow: mid-acceleration ($Re = 2070$) and peak flow ($Re = 5780$). These detailed plots show the ability of high spatiotemporal LBM simulations to capture important details, particularly for high-Reynolds-number flows. At mid-acceleration (figure 19(*a*)), vortex shedding occurs past the open leaflet tips. However, this vortex shedding is coherent and results in two distinct von Karman vortex streets. Although vortex shedding occurs past the sinus expansion step as well, this recirculation region does not interact with the von Karman vortex streets and is not highly disorganized.

For peak flow (figure 19*b*), it is observed that the coherent von Karman vortex streets that shed past the leaflet tips immediately break down into smaller eddies. These detailed fine-scale vortices are not captured in the coarser resolution simulations, instead appearing as a blurred mixing of flow. Similar blurred results for high-Reynolds-number BMHV flow are demonstrated in other coarse resolution experimental and CFD studies of pulsatile BMHV flows (Dasi *et al.* 2007; De Tullio *et al.* 2010). The small eddies in peak flow continue to form and disperse throughout the domain, eventually mixing with each other as well as with vortex shedding in the sinus expansion regions.

It is important to note that these small eddies form downstream of the valve, and persist beyond the sinus expansion. Thus, it is important to maintain high spatial resolution for the entire BMHV domain. For future simulations, these fine-scale features must be resolved to fully capture and understand the pulsatile BMHV flow physics. In addition, for simulations involving blood elements, accurate modelling of these small eddies could play a very important role in damage to blood elements such as red blood cells and platelets. For steady flow comparison of mean flow fields, or qualitative comparison against coarser resolution experimental data, the Kolmogorov scales are not important. However, for the purposes of more accurate BMHV flow modelling or for future blood damage modelling, the inclusion of fine-scale flow features is crucial.

Simulations modelling these problems at high resolution are very expensive, as the domain length scale is of the order of tens of millimetres, and the Kolmogorov

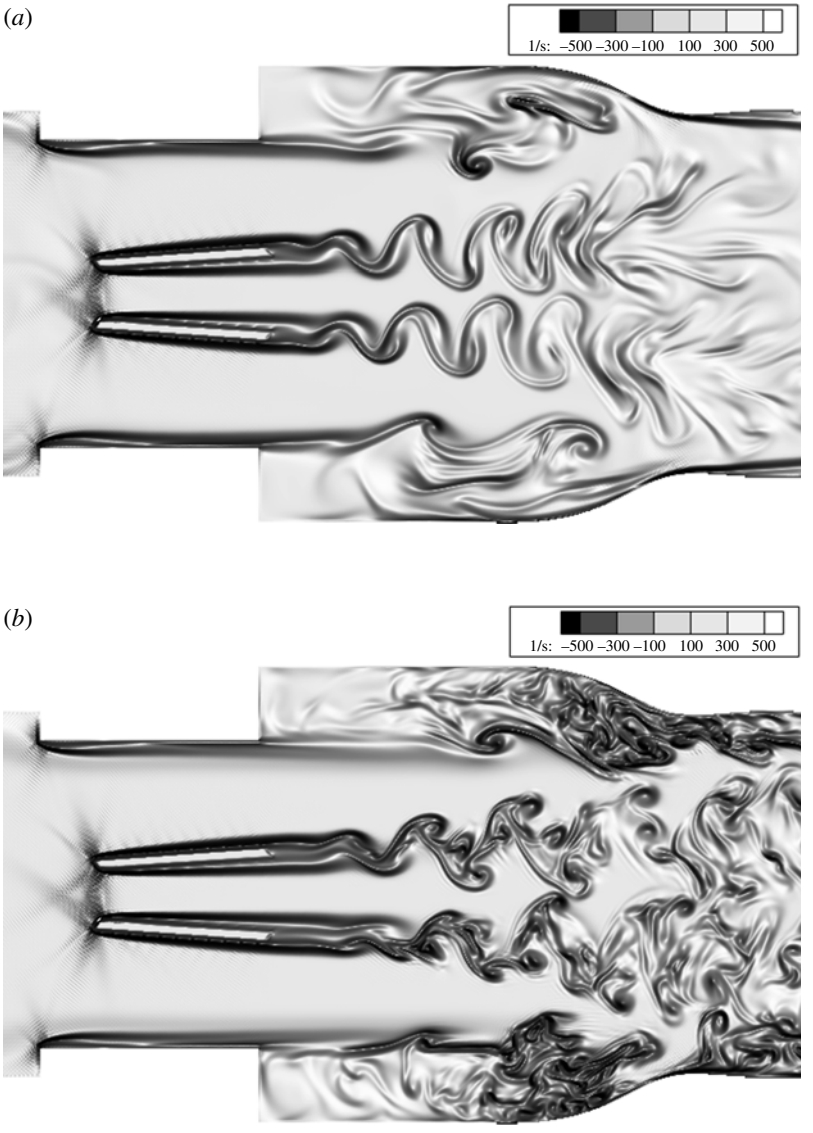

FIGURE 19. Pulsatile flow visualization of (*a*) mid-acceleration and (*b*) peak flow.

length scales are of the order of tens of micrometres. Thus, numerical flow domains would lie in the range of hundreds of millions to billions of fluid grid points. For these large-scale biomedical flow simulations, efficient parallel algorithms are necessary. Although the high-resolution simulation of this study is expensive, it is performed with optimal parallelization and excellent efficiency, and takes less than 20 h to model a cardiac cycle. Thus, future simulations can be performed using this numerical method that can capture the finest details of similar, but novel flows with optimal parallel processing to obtain results in very short times. This can be performed to observe novel cardiovascular flow physics, as well as accurate modelling of blood damage complications in various cardiovascular flows.

4.3. *Turbulence in lattice-Boltzmann modelling of BMHV flows*

For this study and for future studies, a question exists as to whether the entropic LBM is able to capture turbulence in pulsatile BMHV flows. The LBM is a DNS method, and thus matching spatial and temporal resolutions to the small eddy Kolmogorov scales will allow for LBM to capture turbulent flows. The entropic LBM employed in this study has been shown to be able to capture turbulence at $Re = 25\,000$ in free-decaying turbulence simulations (Vahala *et al.* 2008, 2009) by matching the Kolmogorov $k^{-5/3}$ scaling for energy spectra. A separate free-decaying turbulence study showed that entropic LBM could match the $k^{-5/3}$ scaling at $Re = 16\,000$ and 4000, as well as accurately compare to a DNS spectral element method at $Re = 4000$ (Chikatamarla *et al.* 2010).

The Kolmogorov scales for turbulent flow are calculated from mean dissipation rate as

$$\eta = \left(\frac{\nu^3}{\epsilon}\right)^{1/4} \tag{4.1}$$

$$\tau_\eta = \left(\frac{\nu}{\epsilon}\right)^{1/2} \tag{4.2}$$

where η is the Kolmogorov length scale, τ_η is the Kolmogorov time scale and ϵ is the mean dissipation rate. Using a calculated maximum value of $\epsilon = 5.87$ m^2 s^{-3} for peak flow past the leaflet tips (Yun 2014) and a kinematic viscosity of blood of $\nu = 3.5 \times 10^{-6}$ m^2 s^{-1}, this yields Kolmogorov scales of approximately $\eta = 52$ μm and $\tau_\eta = 772$ μs. As the numerical temporal resolution is between 2.4 and 4.8 μs, the simulations are certainly resolving the turbulent time scales for pulsatile BMHV flow.

The higher spatial resolution for the pulsatile flow simulation in this study is 80 μm throughout the entire fluid domain. To the best of the authors' knowledge, no other study (computational or experimental) has resolved full-BMHV pulsatile flow fields at this high spatiotemporal resolution. The pulsatile flow results of this study show the smallest-scale vortices to occur outside of the valve region (figure 19*b*), sometimes several diameters downstream of the valve. Thus, other computational methods that match high spatial resolution only inside the valve are not adequate to accurately capture the entire turbulent flow field. Although the entropic LBM is highly efficient and parallelized, limited computational resources prohibit simulations matching the required Kolmogorov spatial scale throughout the domain. The spatial resolution of 80 μm under-resolves the required Kolmogorov scale by a factor of 1.54.

It is important to note that in the previous entropic LBM studies, turbulence was captured even in cases of under-resolved spatial resolutions. In the studies by Vahala *et al.* (2008, 2009), free-decaying turbulence was captured at $Re = 25\,000$ while under-resolving the required Kolmogorov scale by a factor of 1.24. In the study with comparison to a DNS spectral element method (Chikatamarla *et al.* 2010), the entropic LBM showed excellent matching with both the spectral element method and with the Kolmogorov $k^{-5/3}$ scaling at $Re = 4000$ while under-resolving the spatial grid by a factor 1.43. At $Re = 16\,000$, the spatial grid was under-resolved by a factor of 4 and captured the Kolmogorov $k^{-5/3}$ scaling, although no comparison was performed with the spectral element method.

These previous studies show the ability of entropic LBM to capture turbulence in high-Reynolds-number flows, even while under-resolving the Kolmogorov scales. It should also be noted that the Kolmogorov scales are not strict thresholds required for capturing the smallest eddies, but are more representative of the order of magnitude

of the scales. The study by Yeung & Pope (1989) has also shown that numerical simulations are still able resolve the lower-order moments of turbulent flow if the spatial resolution is within two times the lowest Kolmogorov length scale.

5. Conclusion

The LBM has been used in this study to simulate full-BMHV pulsatile flows with leaflet motion and two-way flow at the highest spatiotemporal resolution to date. These simulations are performed with prescribed leaflet motion and flowrates from experimental data. Quantitative comparison with steady flow experiments show very good velocity matching even at near peak flow, where the flow becomes highly disorganized and unstable. Pulsatile flow simulations show very good agreement with experiments both quantitatively and qualitatively, with good matching of mean flow fields and r.m.s. values and the ability to match key instantaneous flow features at various points in the cardiac cycle. This validates the LBM for use in modelling pulsatile, high-Reynolds-number BMHV flows. This study has also shown the applicability of a numerical time-averaging method for use in comparison with experimental data. Finally, this study has demonstrated the advantages of using LBM to model high resolution, complex biomedical flows with high parallel efficiency in order to capture fine-scale flow features.

The authors have demonstrated in previous studies that LBM in combination with the external boundary force (EBF) method is able to accurately quantify platelet damage in BMHV flows on a smaller scale in the hinges when compared with blood damage experiments (Wu *et al.* 2011; Yun *et al.* 2012). With this study's validation of LBM to accurately model bulk BMHV pulsatile flows, the EBF method can now be included to accurately quantify platelet damage in pulsatile flows throughout the entire BMHV geometry in future studies. The highly parallelized nature of the numerical method allows for efficient simulations at the high spatiotemporal resolution required to capture the finest details of pulsatile BMHV flow, which are important in the accurate modelling of platelet damage in these flows.

Acknowledgements

This research was carried out under a grant from the National Heart, Lung and Blood Institute (HL-07262). Computational simulations were performed using resources from XSEDE: Extreme Science and Engineering Digital Environment (TG-CTS100012). The authors would also like to thank Shiva Arjunon, Neela Saikrishnan and Lucia Mirabella for their useful comments in the development of this work.

REFERENCES

AIDUN, C. K. & CLAUSEN, J. R. 2010 Lattice Boltzmann method for complex flows. *Annu. Rev. Fluid Mech.* **42**, 439–472.

AIDUN, C. K. & LU, Y. 1995 Lattice Boltzmann simulation of solid particles suspended in fluid. *J. Stat. Phys.* **81** (1), 49–61.

AIDUN, C. K., LU, Y. & DING, E. J. 1998 Direct analysis of particulate suspensions with inertia using the discrete Boltzmann equation. *J. Fluid Mech.* **373**, 287–311.

BLACK, M. M. & DRURY, P. J. 1994 Mechanical and other problems of artificial valves. *The Pathology of Devices* **86**, 127–159.

BORAZJANI, I., GE, L. & SOTIROPOULOS, F. 2008 Curvilinear immersed boundary method for simulating fluid structure interaction with complex 3D rigid bodies. *J. Comput. Phys.* **227** (16), 7587–7620.

BORAZJANI, I. & SOTIROPOULOS, F. 2010 The effect of implantation orientation of a bileaflet mechanical heart valve on kinematics and hemodynamics in an anatomic aorta. *J. Biomech. Engng* **132**, 111005.

CHIKATAMARLA, S. S., FROUZAKIS, C. E., KARLIN, I. V., TOMBOULIDES, A. G. & BOULOUCHOS, K. B. 2010 Lattice Boltzmann method for direct numerical simulation of turbulent flows. *J. Fluid Mech.* **656**, 298–308.

CLAUSEN, J. R., REASOR JR, D. A. & AIDUN, C. K. 2010 Parallel performance of a lattice-Boltzmann/finite element cellular blood flow solver on the IBM Blue Gene/P architecture. *Comput. Phys. Commun.* **181** (6), 1013–1020.

DASI, L. P., GE, L., SIMON, H. A., SOTIROPOULOS, F. & YOGANATHAN, A. P. 2007 Vorticity dynamics of a bileaflet mechanical heart valve in an axisymmetric aorta. *Phys. Fluids* **19**, 067105.

DE TULLIO, M. D., CRISTALLO, A., BALARAS, E. & VERZICCO, R. 2010 Direct numerical simulation of the pulsatile flow through an aortic bileaflet mechanical heart valve. *J. Fluid Mech.* **622**, 259–290.

ELLIS, J. T., HEALY, T. M., FONTAINE, A. A., SAXENA, R. & YOGANATHAN, A. P. 1996 Velocity measurements and flow patterns within the hinge region of a medtronic parallel bileaflet mechanical valve with clear housing. *J. Heart Valve Dis.* **5** (6), 591–599.

ELLIS, J. T. & YOGANATHAN, A. P. 2000 A comparison of the hinge and near-hinge flow fields of the st jude medical hemodynamic plus and regent bileaflet mechanical heart valves. *J. Thorac. Cardiovasc. Surg.* **119** (1), 83–93.

FALLON, A. M., DASI, L. P., MARZEC, U. M., HANSON, S. R. & YOGANATHAN, A. P. 2008 Procoagulant properties of flow fields in stenotic and expansive orifices. *Ann. Biomed. Engng* **36** (1), 1–13.

GE, L., LEO, H. L., SOTIROPOULOS, F. & YOGANATHAN, A. P. 2005 Flow in a mechanical bileaflet heart valve at laminar and near-peak systole flow rates: CFD simulations and experiments. *J. Biomech. Engng* **127**, 782–797.

GIERSIEPEN, M., WURZINGER, L. J., OPITZ, R. & REUL, H. 1990 Estimation of shear stress-related blood damage in heart valve prostheses–*in vitro* comparison of 25 aortic valves. *Intl J. Artif. Organs* **13** (5), 300–306.

GRUNKEMEIER, G. L. & ANDERSON JR, W. N. 1998 Clinical evaluation and analysis of heart valve substitutes. *J. Heart Valve Dis.* **7** (2), 163–169.

KEATING, B., VAHALA, G., YEPEZ, J., SOE, M. & VAHALA, L. 2007 Entropic lattice Boltzmann representations required to recover Navier–Stokes flows. *Phys. Rev.* E **75** (3), 36712.

LIM, W. L., CHEW, Y. T., CHEW, T. C. & LOW, H. T. 1994 Particle image velocimetry in the investigation of flow past artificial heart valves. *Ann. Biomed. Engng* **22** (3), 307–318.

MACMECCAN, R. M., CLAUSEN, J. R., NEITZEL, G. P. & AIDUN, C. K. 2008 Simulating deformable particle suspensions using a coupled lattice-Boltzmann and finite-element method. *J. Fluid Mech.* **618**, 13–58.

MANNING, K. B., KINI, V., FONTAINE, A. A., DEUTSCH, S. & TARBELL, J. M. 2003 Regurgitant flow field characteristics of the st. jude bileaflet mechanical heart valve under physiologic pulsatile flow using particle image velocimetry. *Artif. Organs* **27** (9), 840–846.

SIMON, H. A., GE, L., SOTIROPOULOS, F. & YOGANATHAN, A. P. 2009 Simulation of the three-dimensional hinge flow fields of a bileaflet mechanical heart valve under aortic conditions. *Ann. Biomed. Engng* **38** (3), 841–853.

SIMON, H. A., GE, L., SOTIROPOULOS, F. & YOGANATHAN, A. P. 2010 Numerical investigation of the performance of three hinge designs of bileaflet mechanical heart valves. *Ann. Biomed. Engng* **38** (11), 3295–3310.

VAHALA, G., KEATING, B., SOE, M., YEPEZ, J., VAHALA, L., CARTER, J. & ZIEGELER, S. 2008 MHD turbulence studies using lattice Boltzmann algorithms. *Commun. Comput. Phys.* **4**, 624–646.

VAHALA, G., KEATING, B., SOE, M., YEPEZ, J., VAHALA, L. & ZIEGELER, S. 2009 Entropic, les and boundary conditions in lattice Boltzmann simulations of turbulence. *Eur. Phys. J.-Spec. Top.* **171** (1), 167–171.

WU, J., YUN, B. M., FALLON, A. M., HANSON, S. R., AIDUN, C. K. & YOGANATHAN, A. P. 2011 Numerical investigation of the effects of channel geometry on platelet activation and blood damage. *Ann. Biomed. Engng* **39** (2), 897–910.

XENOS, M., GIRDHAR, G., ALEMU, Y., JESTY, J., SLEPIAN, M., EINAV, S. & BLUESTEIN, D. 2010 Device Thrombogenicity Emulator (DTE)-design optimization methodology for cardiovascular devices: a study in two bileaflet MHV designs. *J. Biomech.* **43** (12), 2400–2409.

YEUNG, P. K. & POPE, S. B. 1989 Lagrangian statistics from direct numerical simulations of isotropic turbulence. *J. Fluid Mech.* **207** (1), 531–586.

YOGANATHAN, A., LEO, H., TRAVIS, B. & TEOH, S. 2003 Heart valve bioengineering. *Encyclopedia of Comprehensive Structural Integrity (CSI)*. pp. 795–796. Elsevier Science.

YUN, B. M. 2014 Simulations of pulsatile flow through bileaflet mechanical heart valves using a suspension flow model: to assess blood damage. PhD thesis, Georgia Institute of Technology.

YUN, B. M., WU, J., SIMON, H. A., ARJUNON, S., SOTIROPOULOS, F., AIDUN, C. K. & YOGANATHAN, A. P. 2012 A numerical investigation of blood damage in the hinge area of aortic bileaflet mechanical heart valves during the leakage phase. *Ann. Biomed. Engng* **40** (7), 1468–1485.

ZOU, Q. & HE, X. 1996 On pressure and velocity flow boundary conditions and bounceback for the lattice Boltzmann BGK model. arXiv preprint comp-gas/9611001.